Title
Design of a High Force NdFeB Based Magnetic Tweezers Device Using Iterative Finite Element Analysis with Emphasis on Portability

Permalink

Author
Zacchia, Nicholas Alexander

Publication Date
2014

UNIVERSITY OF CALIFORNIA

Santa Barbara

Design of a High Force NdFeB Based Magnetic Tweezers Device Using Iterative Finite Element Analysis with Emphasis on Portability

A Thesis submitted in partial satisfaction of the

requirements for the degree Master of Science

in Mechanical Engineering

by

Nicholas Alexander Zacchia

Committee in charge:

Professor Megan Valentine, Chair

Professor Kimberly Turner

Professor Brad Paden

September 2014

The thesis of Nicholas Alexander Zacchia is approved.

Megan Valentine

Kimberly Turner

Brad Paden

September 2014

Design of a High Force NdFeB Based Magnetic Tweezers Device Using Iterative Finite Element Analysis with Emphasis on Portability

by

Nicholas Alexander Zacchia

ACKNOWLEDGEMENTS

I would like to acknowledge the hard work of Timothy Thomas (UCSB Internships in Nanosystems Science, Engineering and Technology (INSET) REU program) for his contribution to chapter 2 in particular. He worked on and solved many of the technical issues addressed in that chapter.

I would like to thank Dr. Jerry Hu, UCSB, for assistance with the experimental measurements of the magnetic fields.

Authors gratefully acknowledge the Natural Sciences and Engineering Research Council of Canada (Post Graduate Scholarship to NAZ), the National Science Foundation (through CMMI-1254893, EEC-1062812, and DMR-1121053), and a Burroughs Wellcome Career Award at the Scientific Interface (to MTV).

This thesis is dedicated to my friends in California, to the Great White North and to the best minds of my generation.

ABSTRACT

Design of a High Force NdFeB Based Magnetic Tweezers Device using Iterative Finite Element Analysis with Emphasis on Portability

by

Nicholas Alexander Zacchia

I present the design and characterization of a high force magnetic tweezers device that can apply controlled forces to magnetic beads embedded into soft materials or biological systems, while visualizing the resultant material deformation with microscopy. Using finite element analysis (FEA), I determined the effect of the geometry of the NdFeB magnet array, as well as the geometry of iron yokes designed to focus and shape the magnetic fields. Sixteen shape parameters including the magnet size, positioning and yoke curvature were defined and modeled using open-source magnetic FEA software. Parameter sweeps were performed using custom-written Matlab code. Geometries were optimized for the magnitude of the magnetic field gradient and the length scale over which the magnetic force operated. Once an optimal design was identified, the yoke was fabricated in-house and the FEA validated by mapping the device's magnetic field using a Hall probe. To demonstrate the usefulness of this

approach, I produced a magnetic tweezers device designed for use with optical microscopes available in a core imaging facility. The application demanded device portability and the ability to interface with a number of microscopes, thus imposing significant size restrictions on the magnets used. Iterative FEA delivered an optimal magnet-yoke geometry, which could be mounted to a carriage that advances or retracts on command, giving the operator fine control over the applied force. Such automation allows for rapid force switching, and also allows the effects of long periods of cyclical loading to be determined. The carriage design, automation and implementation were produced in collaboration with a summer intern, Timothy Thomas from the INSET program at UCSB. In future work, such an FEA approach could easily be adapted to a range of design goals/restrictions to create an efficient means of testing possible magnet configurations, while streamlining the design and construction of specialized instrumentation for force-sensitive microscopy.

TABLE OF CONTENTS

LIST OF FIGURES

LIST OF TABLES

I. Design and optimization of arrays of neodymium iron boron-based magnets for high-force magnetic tweezers applications

A. Introduction

Magnetic tweezers devices produce steep magnetic field gradients that enable the controlled manipulation of micro-scale superparamagnetic beads that are simultaneously visualized using optical microscopy. Magnetic tweezers have been particularly useful in applying femto- to nano-Newton scale forces to biological molecules and in characterizing the microrheology of samples that are otherwise difficult to probe.[1-6] These include materials that are intrinsically small and heterogeneous, like biological cells, as well as materials that are difficult to obtain in macroscopic quantities, such as biological protein networks.[7-11] Magnetic tweezers provide a relatively non-invasive way to apply controlled forces to specific locations within a sample of interest, and in comparison to other microscale force manipulation devices, such as optical traps and atomic force microscopes, magnetic tweezers devices are less costly and simpler to implement.

In all cases, the magnitude of the magnetic field gradient and hence the force that can be applied to superparamagnetic beads, is dependent on the flux density and the geometry of the magnetic field produced by a magnetic tweezers device. Large magnetic fields are produced by either use of electromagnets, typically consisting of many turns of a current-carrying wire wrapped around a soft iron core, or by use of pairs of strong rare-earth permanent magnets made of neodymium iron boron (NdFeB). Electromagnetic tweezers are often employed when high-frequency oscillating fields are required, for example, when determining the complex viscoelastic modulus of a material. Additionally, electromagnetic field strength can be dynamically increased by driving higher currents through the device, and the core geometry can be shaped to enhance the field gradients near the sample. Although the fast temporal response is an advantage, the use of large currents can lead to sample heating as well as hysteretic effects that make calibration difficult and necessitate the use of complex feedback and control systems to maintain constant force.[1, 12] By contrast, permanent NdFeB-based magnetic tweezers have no power supply that would cause heating and avoid the need for complex electronic systems, since the only control parameter is the separation distance from the magnetic array to the sample. In most cases, both the magnitude and gradient of the magnetic field $\vec{B}$ decrease as a function of separation distance, leading to a monotonic decrease in force, given by $\vec{F} = \frac{1}{2}\vec{\nabla}\left(\vec{m}(\vec{B}) \times \vec{B}\right)$, where $\vec{m}$ is the induced magnetic moment in the bead. This allows for a robust, one time force calibration based only on magnet array location.[2] Despite these advantages, very few high force designs have been developed, which has limited the use of NdFeB magnetic tweezers devices for materials characterization, particularly for stiff samples, or when small superparamagnetic beads are required. [2, 13, 14]

Although bare NdFeB-based magnetic tweezers generate strong magnetic fields, they fail to produce the large magnetic field gradients needed to produce the same level of forces as electromagnetic devices. However, by attaching yokes with high magnetic permittivity, the magnetic flux from the NdFeB magnets can be concentrated and high field gradients achieved. [3,15-17] In some cases, finite element analysis (FEA) has been employed to compare two or three unique magnet and yoke designs to ascertain the more favorable geometric configuration.[15, 17, 18] However, no prior study has systematically varied the geometric parameters of a NdFeB-based magnet and yoke array to optimize the design for the production of high magnetic field gradients. This work seeks to address the difficulty of obtaining high forces using NdFeB based magnetic tweezers devices by providing an improved methodology for their design, and by specifically optimizing magnet configuration as well as yoke geometry and placement to achieve full magnetic saturation of the yoke and the largest field gradients in regions of interest.

The goal of this research project was to design a small device to apply high forces to microscale samples imaged with high-resolution confocal microscopy without interference to the imaging capabilities of the microscope. In doing so emphasis was put on developing a light-weight and compact design; however, the methodology described here can easily be modified to fit a broad range of design goals.

B. Design Methodology

To analyze the magnetic fields surrounding magnetic tweezers with complex geometries, Finite Element Analysis (FEA) was performed using Finite Element Method Magnetics (FEMM), an open source magnetics solver.[19] FEMM was used to perform magnetostatic analyses of particular geometries, solving for the magnetic field strength $\vec{H}$ and magnetic flux density $\vec{B}$ in the 2-D horizontal plane of symmetry. The out-of-plane depth of the simulation can be specified for the geometry, which enables a quasi 3-D analysis. Such FEMM models have only one free parameter, corresponding to the actual magnetization of the magnets used, which depends on the magnet manufacturing technique and is not necessarily known *a priori*.[20]

The initial FEMM input geometry for the magnet and yoke was based on a previous high force magnetic tweezers design, which used two rectangular NdFeB magnets placed side-by-side with their magnetic poles aligned in parallel, and with two horn-shaped soft-iron yokes to concentrate the magnetic flux at the yoke tips.[3] Several geometric regions were defined according to their proximity to the magnet array and each was assigned a FEA mesh size varying from 0.1 to 1.2 mm, depending upon the location.

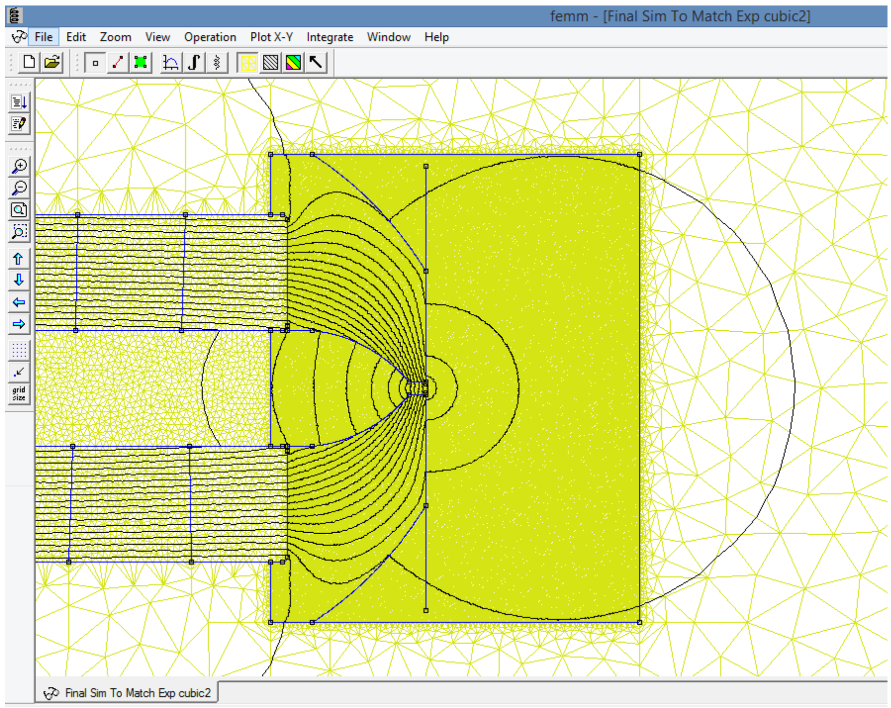

Figure 1: FEMM input for the magnet and yoke geometry showing the meshing used for FEA simulation.

Regions nearest to the magnets and yokes, and at the location of the sample plane were given the finest mesh. By comparison, the magnet size in the final design is approximately 9.5 mm by 28.5 mm. The optimal mesh size was selected to be the largest size that gave >98% agreement with an identical simulation performed with a mesh twice as fine.

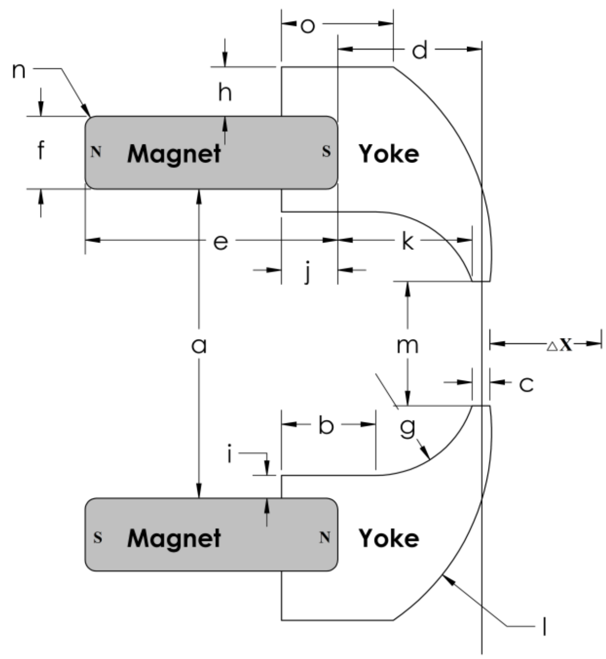

Figure 2: Schematic layout of a magnetic tweezers device with horn-shaped yokes. Letters represent different parameterized variables in the geometry. Table 1 lists each geometric parameter and indicates the effect of varying that parameter on the $\nabla_x|\vec{B}|$. The line labeled Δx represents the contour along which the $|\vec{B}|$ values are tabulated. A sample would be placed normal to the distal end of this contour.

To understand the effects of magnet and yoke geometry on device performance, every aspect of the magnet and yoke geometry was parameterized and then systematic changes to each parameter were made independently to verify their effects on the magnetic fields produced by the device (Figure 2). To qualitatively compare the various simulations, the magnitude of the $\vec{B}$ field was plotted as a two-dimensional (2-D) density plot, providing insight into how the magnet and yoke geometry influence the distribution of field lines around the device.

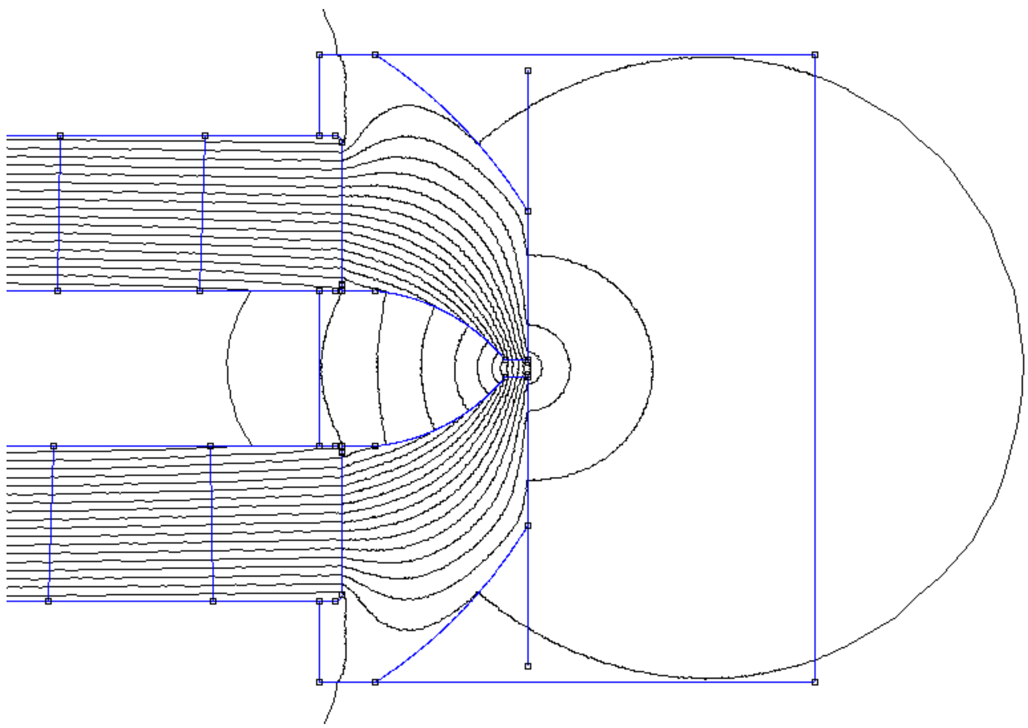

Figure 3: FEMM output showing the magnetic field lines around a sample geometry.

Additionally, quantitative values of the magnitude of the $\vec{B}$ field were plotted for a 1-cm long path extending from the midpoint between the tips of the magnetic tweezers device and extending away from the magnets into the area where a sample would be located (given by Δx, as in Figure 2). From these data, a figure of merit was developed to quantitatively compare the performance of each magnet and yoke configuration based on a linear fit to $|\vec{B}|$ versus the magnet-sample separation distance Δx (Figure 2). The slope of the fitted line provides a locally-averaged estimate of $\nabla_x|\vec{B}|$, which in the limit of large magnetic fields (when the bead's magnetic moment saturates to a constant value) is directly proportional to the applied force. The calculation of $\nabla_x|\vec{B}|$ also provides an estimate of the distance over which the applied force remains high enough to be experimentally useful. While this may not be the ideal metric for every application, it allows for the rapid comparison of various design iterations, and simplifies the optimization process. A characteristic length, L_o, is defined as the distance over which $\nabla_x|\vec{B}|$ remains linear to within an r-squared value of 0.95. We find that for geometries that produce the highest gradients, $|\vec{B}|$ declines rapidly. We require a minimum value of L_o to account for the physical separation between the tweezers and sample due to the cover slip, flow tubes, etc. By enforcing a minimum L_o value during the design optimization, we ensure that the design will generate high forces over experimentally useful distances. Of course, using other optimization criteria are possible for cases with different application needs.

In practice, a large number of designs (~5000) were tested and compared. This necessitated the use of batch processing to facilitate parameter sweeps and post-processing of the simulation data. This was done using custom-written MATLAB code interfaced to FEMM contained in Appendix A. For each simulation, $|\vec{B}|$ versus Δx was tabulated, plotted and overlaid with the linear fit that provided $\nabla_x|\vec{B}|$. For each set of geometric parameters, the values of $\nabla_x|\vec{B}|$ versus x, L_o, and the 2-D density plot of $|\vec{B}|$ were recorded. In all cases, parameters were swept from the minimum machinable values (which are in some cases zero) to an upper bound that was determined empirically, and informed by the results of past parameter sweeps and geometric limitations imposed by our desire to interface the device with a high-resolution confocal microscope.

Table 1: List of geometric parameters that were varied in design, with description of primary effects on $\nabla_x|\vec{B}|$, range of values tested using FEA and optimized value.

Parameter	Description	Tested values (mm)	Optimized value mm
Category 1: $\nabla_x\|\vec{B}\|$ decreases as parameter value increases			
h	Outside yoke thickness	0.2 - 10	5 [d]
i	Inside yoke thickness	0 - 5.8	0
j	Yoke depth	0 - 25	1.4
k	Distance to yoke tip	3 - 15	10
l	Outer yoke angle	1 - 101 degrees	30.5 degrees [c]
m	Tip separation	0.2 - 2	1 [e]
Category 2: $\nabla_x\|\vec{B}\|$ asymptotically increases, but gains diminish due to magnetic saturation of yokes			
e	Magnet length	15.3 - 45.3	28.575
f	Magnet width	6.3 - 21.3	9.525
g	Inner yoke angle	2 - 111 degrees	21 degrees [c]
Category 3: Optimal value exists to maximize $\nabla_x\|\vec{B}\|$			
a	Magnet separation	4 - 55	9.525
b	Inside yoke length	1.25 -10.5	2 [a]
c	Yoke tip length	0.1 - 5.1	1.35
d	Depth of yoke cut	10 - 14.8	11.35 [b]

Category 4: No effect			
n	Magnet edge radius	0.1- 3.1	0.3
o	Outside yoke length	0 - 8	3.4

[a] Strongly coupled to *k*. The actual value used in the final design was tuned in conjunction with *k* and is not simply the maxima as shown in Appendix B.

[b] Strongly coupled to *c, g, i, k* and *l*.

[c] Once parameter *d* was optimized, these parameters could be varied significantly with little to no effect on the figure of merit.

[d] Strongly coupled to *a*.

[e] Small values of *h* shift the region of high gradient closer to the yoke tips. A minimum must be established in order to produce meaningful forces in the vicinity of a sample, which is usually separated from the yoke by a cover slip or flow cell of finite thickness. Additionally, in some designs, the illumination light passes through the tips to the sample. Here, a minimum of *n* = 1 mm was chosen.

C: Results

1. Finite Element Analysis

Through a systematic approach to design optimization, it was found that the gradient of the magnetic flux is affected by many of the geometric parameters, and several general classes of response were observed. (see the summary in Table I, and detailed FEA results in Figure 4 and Figure 5). In some cases, as the parameter value increases $\nabla_x|\vec{B}|$ decreases (Category 1), in others $\nabla_x|\vec{B}|$ asymptotically increases, but gains diminish due to magnetic saturation of yokes (Category 2), or an optimal value exists to maximize $\nabla_x|\vec{B}|$ (Category 3), and in some cases there is no effect (Category 4).

For Category 1 parameters, $\nabla_x|\vec{B}|$, and thus the magnetic force, decreases as the parameter value increases. As our application required large forces, a minimum value was desirable for these parameters. In practice, assembly and manufacturing constraints determine the chosen values for h, k and m. By contrast, increasing the parameters e and f that describe the magnet length and width, respectively, initially increase the values of $\nabla_x|\vec{B}|$, but gains quickly diminish due to the induced magnetic saturation of the yokes (Category 2). To achieve high force, yokes are required to focus the magnetic flux and increase the value of $\nabla_x|\vec{B}|$. However, there are limits to the gains that can be achieved in this manner. Once the yoke material reaches magnetic saturation, further gains cannot be made by increasing the magnetic field strength $\vec{H}$, as this no longer has any effect on the magnetic flux density, $\vec{B}$, within the material. Once saturation is achieved, many individual parameters can be varied slightly without any effect on Grad $\vec{B}$, most notably e, f, g, h and k. In practice, for Category 2 parameters, a threshold value was identified, above which there was little advantage to be gained, and this threshold value was considered to be optimal. The exact magnet size for the fabricated device was then selected based what was commercially available.

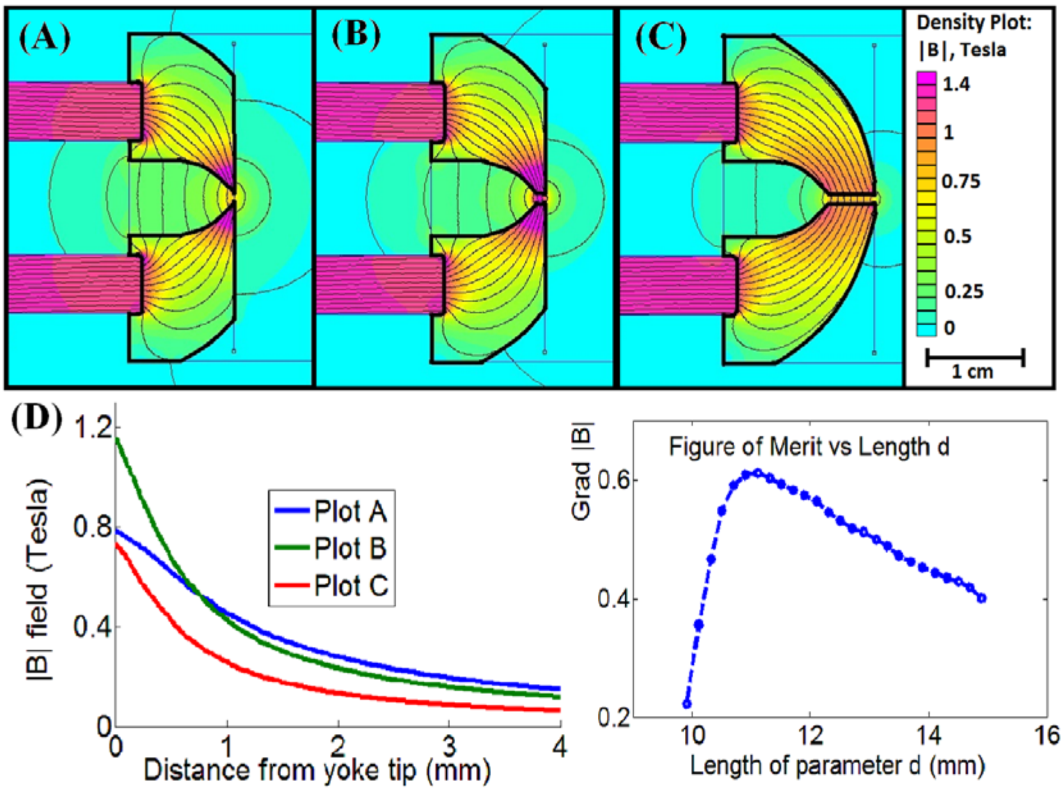

Figure 4: (A-C) - Output of iterative FEA : The depth of yoke cut (parameter d) was varied from 9.9 mm to 14.9 mm in increments of 0.2 mm. Panels show the depth of cut at (A) 9.9 mm (B) 10.9 mm (C) 14.9 mm. (D) $\nabla_X|\vec{B}|$ for each of the three previous panels. (E): As the cut length (parameter d) grows, $\nabla_X|\vec{B}|$ first increases to an optimal value, then decreases monotonically (Category 3).

Parameters in Category 3, exhibit a non-monotonic response, in which $\nabla_x|\vec{B}|$ first increases, then decreases as the parameter value is increased. An example of this type of response is shown in Figure 4. For our high-force applications, parameter values giving maximal values of $\nabla_x|\vec{B}|$ were considered optimal. We found the parameters in Category 3 were especially sensitive to changes in the values of each other. In practice, once optimal values for the parameters in Categories 1 and 2 were found, the Category 3 parameters were swept through individually or in pairs in order to determine their optimal value, then these values were held fixed while the next individual or pair of parameters was swept through.

Our overall design goal is to increase the local gradient, $\nabla_x|\vec{B}|$ as much as possible in the region just beyond the yoke tips, where the sample of interest is placed. One potential complication in this optimization is the coupling between $\nabla_x|\vec{B}|$ and L_o. For example, it is possible to maximize the magnetic force by minimizing parameter m, the yoke tip separation; however, small values of parameter m also correspond to a very short linear range. As m increases from zero, the maximum gradient achieved diminishes rapidly while the peak $\nabla_x|\vec{B}|$ shifts towards larger values of Δx. In other words, the smaller the value of m, the higher $\nabla_X|\vec{B}|$ can be achieved, but only over very small distances in the tens of microns. This type of coupling is important when considering experimental constraints, such as the finite thickness of flow cells or coverslips that necessarily lie between the tweezers and the sample under investigation. The optimal value of *m* is thus determined by the experimental setup for which the tweezers is being designed.

To develop a better understanding of the physical origins of the geometric optimization, we combine quantitative information from the various parameter sweeps with the distribution of field lines and magnetic flux density obtained from the density plots. This allowed us to explore large scale, non-perturbative changes to the magnet and yoke geometry beyond simple parameter sweeps. These included completely different yoke shapes or the inclusion of more than two magnets to create and direct the field gradient. An example of this qualitative analysis is given in Figure 5 with regard to the yoke depth (parameter *j*). Sweeping through the range of values for *j* showed that the highest gradients at the yoke tips were obtained at minimal values of yoke depth (Category 2 response). The density plots allow us to understand why this is the case: as the yoke depth increases, magnetic flux is directed away from the yoke tip, and diverted to the opposite end of the selfsame magnet (Fig. 3).

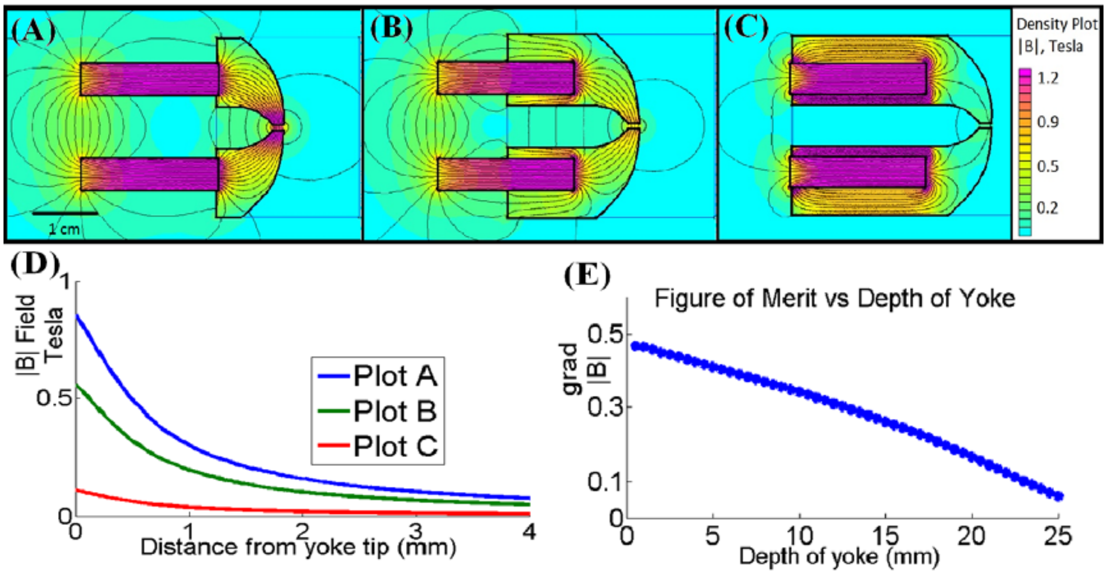

Figure 5: (A-C) - Output of iterative FEA : The yoke depth (parameter j) was varied from 0.4 mm to 25.4 mm in increments of 0.5 mm. Panels display the density plots of magnetic flux density, $|\vec{B}|$, at various yoke depths: (A) 0.4 mm (B) 12.9 mm (C) 25.4 mm. Contours in black indicate magnetic flux lines. The pink colors indicate regions of high $|\vec{B}|$ while teal indicates lower $|\vec{B}|$. (D) $|\vec{B}|$ plotted against ΔX for each of the three previous panels. (E): As the yoke grows, Grad $\vec{B}$ plotted against the depth of the yoke. Grad $\vec{B}$ decreases as yoke depth increases. The density plots show how flux lines begin to deflect backwards towards the other end of the selfsame magnet, limiting the maximum magnetic flux achieved at the yoke tips. Similar parameter sweeps are performed for all shape parameters and provided in supplemental material.

Further analysis of the density plots allowed us to investigate the best approach to directing the field lines at the rear of the device. Prior work demonstrated that placing a soft iron bar behind the magnets, opposite the yokes, enhanced the field gradients along Δx.[3, 17] In this work we found that even larger gradients could be achieved by adding a third magnet and 2 steel turning pieces to the back end of the magnetic tweezers device (Figure 6). This design effectively created a closed path for the magnetic flux emanating from the back end of the tweezers device, and ensured that no stray flux from the front end of the device was directed backwards and away from the sample.

Qualitative study of the design parameters also indicated that angles swept out by l and m were of little consequence in the final design, and in fact, cutting the front of the yokes, as denoted by parameter o improved the gradient achieved, simplified machining, allowed samples to be butted up against a flat surface and helped ensured yoke tip saturation with less sensitivity to the inner and outer yoke radius (parameters g and i, respectively). Detailed figures on the dependence of $\nabla_x|\vec{B}|$ on parameters a through o as they vary can be found in Appendix B.

2. Fabrication, Testing and Model Validation

Based on our iterative FEA approach, we determined the optimal geometry for a compact but high-force magnetic tweezers device. We then fabricated and tested this device both to validate our finite element modeling, and to produce a working prototype. The final magnetic tweezers designs uses seven cubic N52 NdFeB magnets, each 3/8 inch (9.525 mm) on each side (available from Applied Magnets, Plano, TX, USA part number NB010-N52). The magnet-yoke array incorporates two 3/8 inch cubes machined from 1010 steel that operate as field turning agents at the rear of the device, and 2 custom-machined horn-shaped focusing yokes, also made from 1010 steel. The yoke material was chosen for its relatively high magnetic saturation as well as its availability and ease of manufacturability. These elements are assembled and housed in a custom-designed and machined aluminum housing which provides mechanical support to the yoke and magnet elements without interfering with the magnetic fields produced (Figure 6).

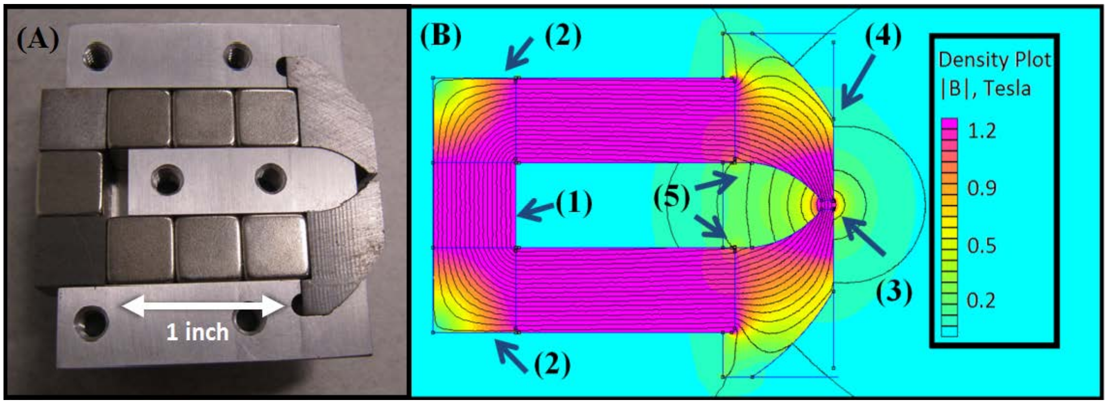

Figure 6: (A): Picture of final magnetic tweezers device. The elements of the magnet-yoke array, described in FIG. 4 (B), are contained within an aluminum housing. In actual implementation, 3 cube magnets replace one long rectangular magnet. Validation showed no significant error introduced by using cube instead of rectangular magnets. (B) FEA output of final design. Critical design elements include: (1) A single cube magnet placed at the back end of the device to create a closed path for the magnetic flux lines; (2) Soft iron cubes (1010 steel) to direct magnetic flux between magnet arrays; (3) With this design, magnetic saturation of yoke material at tips is achieved; (4) The blunted edge of the yoke tips increases $\vec{\nabla}|\vec{B}|$; (5) Minimal inside yoke depth and thickness is used to avoid the diverting magnetic field from the sample plane.

The output of the magnetic tweezers device was characterized using a F.W. Bell 5170 series gaussmeter with transverse probe, (resolution 0.001 T and a full range of 0-2 T). The magnitude of the $\vec{B}$ field was measured at regular intervals (25.5 μm, given by 1/10 of a rotation of a calibrated micrometer stage screw) from the yoke tips along the Δx direction (Figure 7). This probe passes through the mid-plane of the central axis of the yoke tips, which are 3/8 inch (9.525 mm) thick. This measurement was then repeated with the gaussmeter probe placed flush with the underside of the magnet array. The measurements from this bottom plane were compared against the mid plane values and showed an agreement within 2.5%, indicating good uniformity in the magnetic fields over these distances. This indicates that the force calibration of the magnetic tweezers device would be insensitive to minor changes in the out of plane location of a sample bead, simplifying experiments.

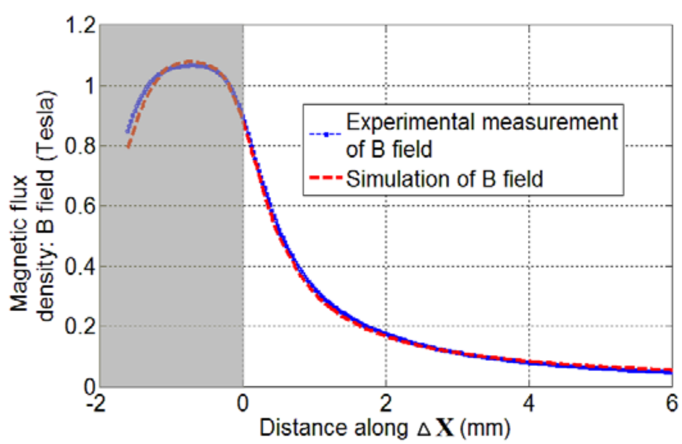

Figure 7: |B| field determined from FEA (red dashed line) and experimental measurement (blue dotted line) plotted along Δx. The position Δx = 0 indicates the position at which the yoke tips and sample are in contact. The gray area is an exclusion zone located between the yoke tips where samples likely could not be placed. However, the small gaussmeter probe could be fit between the yoke tips. The FEA has one free parameter to account for the magnetization of the magnets used. The residuals between the simulated and measured data were less than 1% of measured values.

These experimental data also allow quantitative comparison to the field amplitude values given by the finite element modeling. For simplicity the FEA simulations were performed using one solid rectangular magnet rather than three cubic magnets, with no significant change in the calculated $\vec{B}$ field values, as shown in Figure 4B. When performing the FEA, there is one free parameter: the magnet coercivity (units: A/m), which is an indicator of the magnet strength. As this value varies magnet to magnet, and with production techniques, this parameter must be determined through experimental validation. This can be accomplished by measuring the $\vec{B}$ field around the bare magnet using a gaussmeter, and then using the experimentally-determined value of coercivity in the FEA, or by fitting the uncalibrated FEA output to the experimental data with the magnet coercivity as a free parameter. In this work, the second approach was used.

When we compare the values of $|\vec{B}|$ predicted by FEA, after scaling by the fitted value of coercivity, to those measured experimentally, we find the average root mean squared difference to be less than 1% of measured values. From the values of $|\vec{B}|$ determined by FEA or experiment, it is possible to numerically calculate $\nabla_x|\vec{B}|$. For our final design, we find that the gradient, and thus the force, is highest near the yoke tips, with the maximum force occurring at ~100 µm from the front face of the magnetic tweezers device (Figure 8).

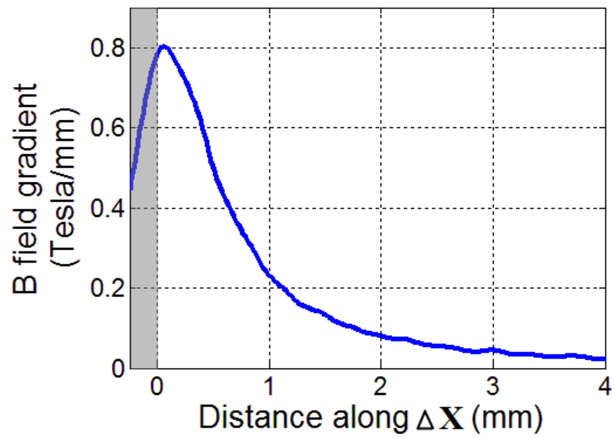

Figure 8: Plot of $\nabla_x|\vec{B}|$ versus Δx. The data was obtained by plotting the local derivative of the experimentally measured values of $|\vec{B}|$ after applying a moving average filter on the data to smooth experimental error caused by the coarse measurement intervals when compared to the measured values of $|\vec{B}|$ near the outer reaches of Δx. The experimental data indicates that the maximum gradient occurs at ~100 µm from the yoke tips. This distance to the point of highest gradient can adequately accommodate most sample containers, ensuring that the highest forces are generated near the inner sample chamber surface.

D: Discussion

This work investigated the optimization of NdFeB based magnetic tweezers devices by systematically studying the effects of geometry and configuration on the ability of a device to generate a large $\vec{B}$ field gradient. The

FEA-guided design approach we employed was fast and efficient, allowing us to accurately simulate thousands of potential geometries. This type of approach can be used to optimize instruments for a range of applications. Since the magnets and yokes are relatively easy and inexpensive to produce, this approach could lead to devices tailored to produce well understood forces at particular locations of interest, as well as devices that develop high forces while conforming to existing geometric constraints, for example to allow mounting to existing experiments or optical imaging platforms.

One important outcome of this work is establishing that there is a clear limit to the performance gains that can be made by simply using larger NdFeB magnets. Although the total magnetic field strength increases with NdFeB volume, we find that the magnetic field gradient produced asymptotes with magnet size, in agreement with suggestions from prior work.[17] This limit arises because high field gradients are generated using metal yokes with high magnetic permeability and a high magnetic saturation point, and once the yoke tips become magnetically saturated, it is very difficult to further increase $\vec{\nabla}|\vec{B}|$.

Importantly, these design lessons apply equally to electromagnetic tweezers devices, which also use yokes and/or pole pieces with inherent material limitations. This suggests that, given the same yoke materials, properly optimized NdFeB-based magnetic tweezers should have similar force performance as their electromagnetic counterparts while avoiding the need for complex control systems. At the same time, simply driving higher currents through electromagnetic devices will not indefinitely increase the force applied to superparamagnetic beads.

Finally, this work has shown that magnetic saturation of yokes can be developed with a relatively small magnet array. The ability to develop very high forces using relatively small cube magnets (each < 1 inch per side), gives NdFeB based magnetic tweezers a degree of versatility and portability that many current tweezers configurations lack.

E: Conclusion

Using FEA approaches, we investigated role of the geometry and configuration of NdFeB magnet arrays in determining the performance of magnetic tweezers devices. This work has led to an improved quantitative and qualitative understanding of the optimal designs for high force applications. The best practices of this work can be applied to the design of magnetic tweezers devices for a range of specific applications.

II. Designing for device portability and automation

Two goals associated with this project were to create a magnetic tweezers device with the versatility to be used with a range of visualization techniques and the ability to automate the positioning of the magnetic tweezers device to ensure accuracy and repeatability of magnet positioning. Automation is made more challenging by the fact that this is a portable system, which means that actuation, power, sensing and control system must be accomplished by elements that can stand alone. In this respect, NdFeB based magnetic tweezers are clearly advantageous over electromagnetic tweezers because they free the device from bulky power supplies that need to be plugged into an electrical outlet.

Versatility means the ability to interface with a number of different types of microscopes so that various imaging techniques can be used to image the microstructure of soft polymeric materials as the tweezers apply localized forces to the same regions of the sample. A requirement of the magnetic tweezers device is that it be interfaced to a confocal microscope available in the shared microscope facilities found in the Neuroscience Research Laboratory core labs at UCSB. This required the device to be self-contained, portable and to require no permanent changes to the microscopes on which it is mounted. Ideally a user could bring the magnetic tweezers device into a shared facility, easily set it up on a microscope, perform experiments and then leave with the device, leaving the microscope exactly as it was found. This goal was accomplished through the implementation of a small, versatile carriage system which allows the device to be mounted to a range of microscope stages without interference.

Automating the positioning of the magnet array with respect to the experiment sample was deemed necessary to improve device usability and the quality of the data obtained with the instrument. Automation here is defined as the ability to displace the magnet array by known amounts in a precise, repeatable way without manual manipulation of the device or its carriage.

Previous iterations of a portable magnetic tweezers device were manually operated, which was cumbersome in practice.1 In this design, automation and accuracy was accomplished by implementing a linear actuator to move the magnetic tweezers, controlled by a microcontroller and powered externally though a battery. The linear actuator was connected to a telescopic sliding assembly to relieve stress on the actuator and to maintain side to side rigidity. The magnet and yoke array, the actuator and the telescopic slide were mounted in a 3-axis micrometer stage to ensure accurate positioning of the magnets.

A. Device Compatibility

The requirement for the magnetic tweezers device being produced was that it work with an existing confocal microscope. A main interest in using magnetic tweezers devices comes from the ability to pair a tweezers device with a high powered imaging tool. This allows the researcher to gain a deeper understanding of the dynamics of soft matter by being able to actually see what happens to the material as force is being applied to it. This is an advantage of magnetic tweezers since their non-contact force exertion leaves ample space for imaging. The more sophisticated the imaging technique, the more information can be gathered from the tool.

This is also why it is desirable to build a magnetic tweezers device that is portable. Portability means that high cost microscopes do not need to be designated solely for the use with a particular magnetic tweezers device. Similarly, portability means that if a tweezers device is optimized for a particular soft matter system then it can be interfaced to a variety of imaging tools which can allow for a more in depth study.

For the purpose of this research, the magnetic tweezers device was designed to work primarily with an Olympus Fluoview 1000 Spectral Confocal microscope located in the shared NRI / MCDB Microscopy Facility located in the Bio 2 building at the University of California Santa Barbara. The confocal microscope of interest has limited usable space around its objective lens due to a number of microscope elements crowding the area. The most important obstacle to build around was an environmental box installed on the confocal microscope in 2012-2013. This environmental box was installed in order to maintain specified atmospheric conditions around a sample. This is especially important when dealing with sensitive biological samples and living tissue. The environmental box limits the size and location of the device carriage and makes it difficult to mount and access the device. Although not all high powered imaging tools have an environmental box, designing for it means creating a more versatile tool. In addition to the environmental box there is also a condenser lens above the microscope stage, see Figure 9 and Figure 10. This condenser lens is similar to condenser lenses on a number of microscopes. The limited distance between the microscope stage and condenser lens places limitations on the height of the magnetic tweezers setup.

In addition to these size constraints, the installation and operation of the magnetic tweezers device should not interfere at all with the existing system. The microscope stage of the confocal microscope has a limit as to the amount of weight it can support, which is 10 pounds. More weight than this can disrupt the stage`s ability to move accurately. Thus a weight restriction of less than 10 pounds was placed on our device.

Figure 9: Confocal microscope in the NRI / MCDB Microscopy Facility at UCSB. The microscope is outfitted with an environmental control box which places limits on the size and shape of any device interfaced with the microscope.

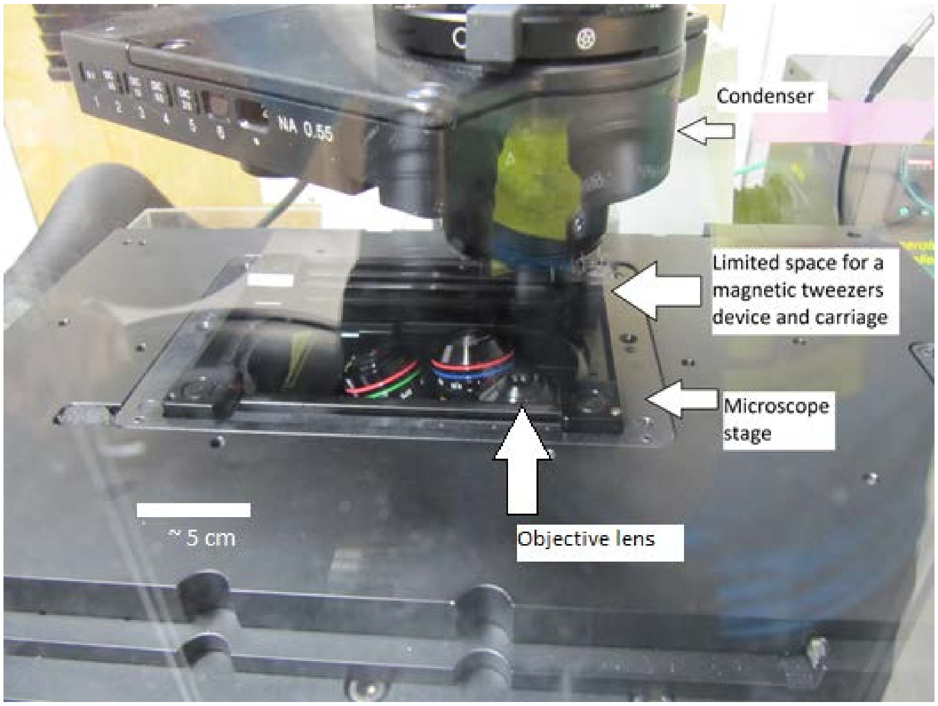

Figure 10: Close up view of the confocal microscope. The objective is visible beneath the microscope stage. When using a magnetic tweezers device, the sample being studied would be placed on the stage platform, just above the objective lens and the tweezers device would have to butt up against the sample as shown schematically in Figure 11. The limited space between the microscope stage and the condenser above place severe size restrictions on the magnetic tweezers device and the carriage used to mount it.

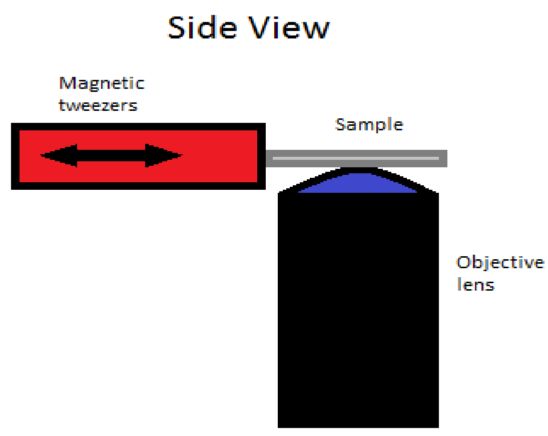

Figure 11: Schematic side view of the experimental setup. A sample, contained in a capillary tube or on a glass slide sits on top of the objective lens. The magnetic tweezers device butts up against the sample from the side. It can then be moved away from the sample in order to modulate the force applied to the beads within the sample.

The final mounting solution for the magnets, micrometer stage and motor consisted of a modular mounting setup which could be bolted onto a range of microscope stages. Custom brackets were designed and fabricated to facilitate interfacing the various components of the device which include the magnet and yoke array, the actuator, the telescopic slide and the 3-axis micrometer stage. Figure 12 shows the final assembly of the portable magnetic tweezers design.

Figure 13 shows a mockup of how the assembly is actually attached to the confocal microscope. The assembly is bolted to existing screw mounts in the microscope stage. The total weight of the magnetic tweezers assembly is approximately 3.5 pounds. This is well below the 10 pound maximum recommended weight that can be applied to the microscope stage.

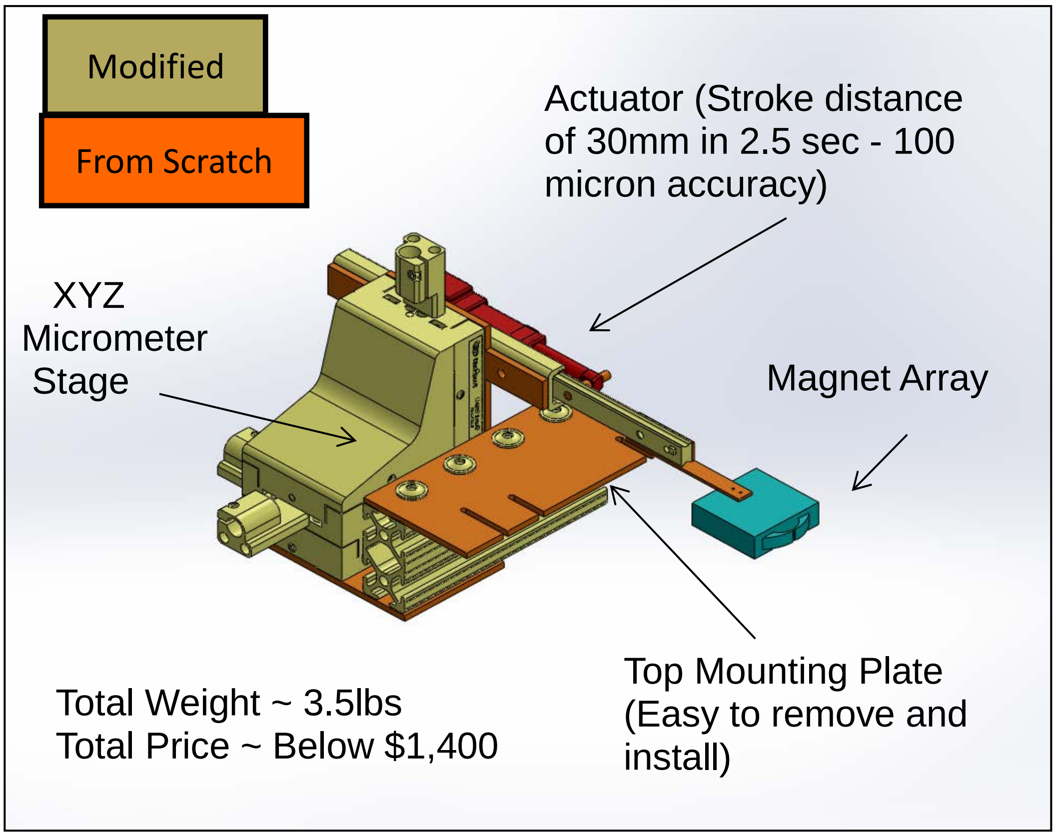

Figure 12: Final assembly of the portable magnetic tweezers device. Components in orange were designed and machined in house using aluminum. Components in gold were purchased and modified. Purchased items are listed in Appendix C. Modifications were mostly limited to cutting pieces to size, drilling and tapping positioning holes. The actuator is in red and in blue the magnet array as discussed in Chapter I. Design and optimization of arrays of neodymium iron boron-based magnets for high-force magnetic tweezers applications.

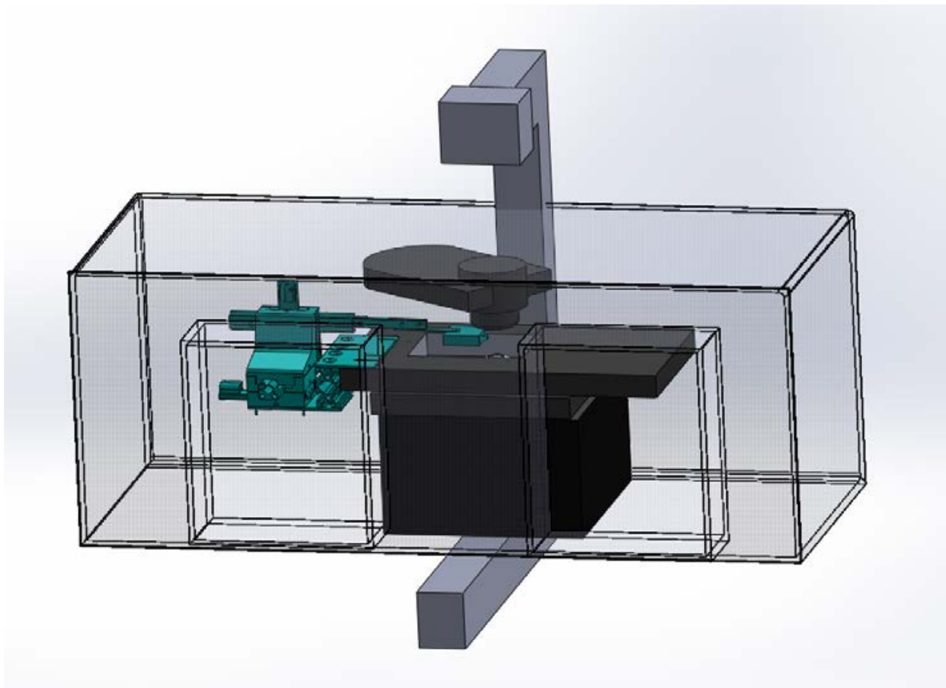

Figure 13: CAD mockup of the portable tweezers device mounted on the confocal microscope. The top mounting plate (shown in Figure 14) was designed so that its slots line up with threaded mounting holes in the stage used on the confocal microscope. If a different stage is used with different hole geometry, the mounting plate on the tweezers device can be modified or replaced.

The components of the mounting assembly are designed to provide course adjustment of the magnet array position with respect to a sample. Fine adjustment is provided by the 3 axis micrometer stage which provides sub-micron sensitivity. Additionally, the actuator mounted to the magnet array provides useful positioning for force application. A full parts list is included in Appendix C. The final assembly for the portable magnetic tweezers device is shown in Figure 14.

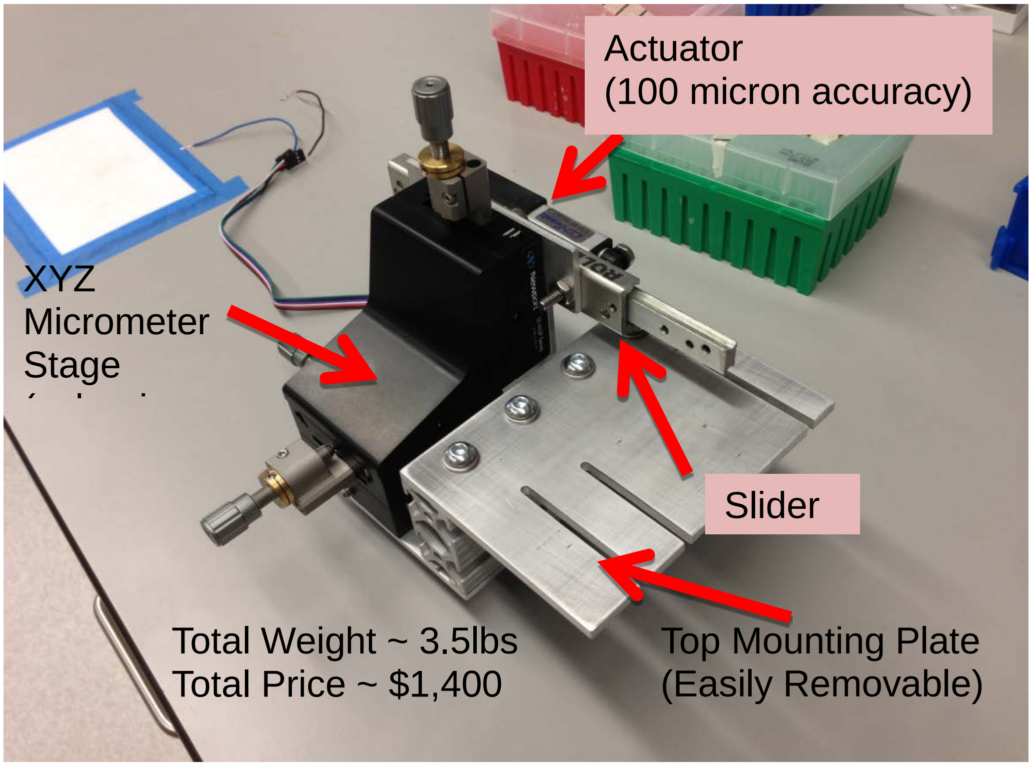

Figure 14: Final assembly for the portable magnetic tweezers device.

B. Device Automation

A second goal of this portable magnetic tweezers device was device automation. Automation here is defined as the ability to displace the magnet array by known amounts in a precise, repeatable way without manual manipulation of the device or its carriage. The force applied to a bead within the sample is directly correlated to the distance from the bead to the magnet. Thus, the ability to position the magnet precisely and accurately gives the experimenter fine control over the force applied to that bead. The automation of the device was deemed important for the repeatability of force application as well as for the ability to run longer experiments.

For example, one experiment in which automation becomes important is the effects of cyclic stress on crosslinked networks. In this type of experiment, a particular bead, or set of beads would be imaged. A force would then be applied to those beads for some finite time and then turned off. Once this sequence of force on – force off was imaged, it would be repeated dozens or hundreds of times. This could give experimenters insights into how stress-strain relationships change over time, how different cross linked samples respond to cyclic loading, or if these networks have any self-healing mechanisms which would allow them to repair themselves between successive force applications.

By using an automated platform which allows for accurate and reproducible force application, many new possibilities are opened up for experimenters. This could include experiments that step through several levels of force as the experiment progresses.

Automation of the device could have been accomplished in two basic ways, as a completely stand-alone device, or interfaced with some other portable device, such as a laptop computer. For maximum portability and versatility, it was decided that a totally autonomous system was preferable. This entailed battery operation, onboard actuation, onboard sensors and onboard signal processing.

The actuation and sensing is accomplished by a linear actuator unit with an embedded internal position controller. The motor used is a Firgelli L12 - option I stroke: 30mm, gear ratio: 100:1, voltage: 6V. The positional accuracy of the actuator is listed as 200 microns. End to end accuracy (the ability to get to the same position at the end of the actuator stroke) was measured to better than 5 microns. The actuator data sheet is included in Appendix D.

The actuator is powered by a 6 volt circuit, however positional control of the actuator is provided by a 5 volt pulse width modulation (PWM) signal which can be provided by a suitable microcontroller. A picture of the linear actuator used is provided in Figure 15. Wiring for the actuator can be found in the data sheet in Appendix D.

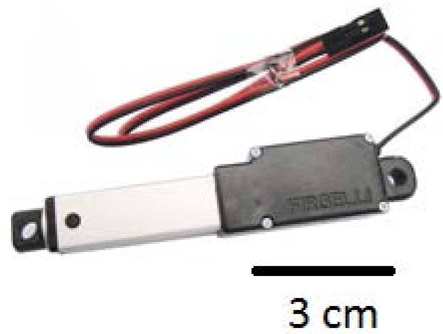

Figure 15: Firgelli linear actuator used to automate the portable magnetic tweezers device.

The actuator is powered by 6 volts which necessitated a battery of at least 6 volts. A 6 volt carbon zinc battery was chosen to power the entire circuit because of its low cost and because it was readily available. If significant use is made of the tweezers device, a rechargeable 6 volt battery can be used instead.

The signal used to position the actuator is a 5 volt pulse width modulation (PWM) signal. This can be provided by a range of microcontrollers. In choosing a microcontroller, a high resolution on the PWM output signal was desired to provide better resolution on the position of the linear actuator. Additional requirements were ease of programming and the size of the board's flash memory (which defines how large a program the board can retain in memory). The microcontroller chosen was the Leaflabs Maple Rev 5 board shown in Figure 16, available through sparkfun.com (https://www.sparkfun.com/products/10664).

The board features 16 bit resolution on PWM pins and 128 kb of flash memory. The board is serviced by a development environment which allows the user to program the board in much the same way as an Arduino microcontroller. Full information, data sheets, downloads and user information, too long to include here, is contained in several libraries found at http://leaflabs.com/docs/index.html

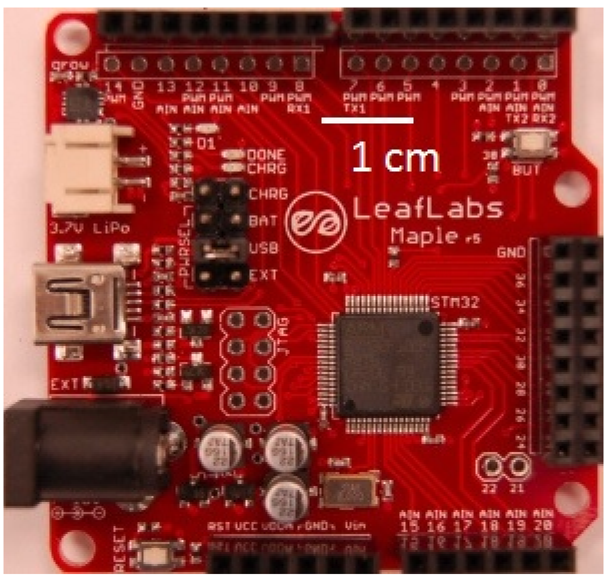

Figure 16: The Leaflabs Maple Rev 5 microcontroller board used for the portable magnetic tweezers device.

The Maple board runs on 3.3 volts. It has onboard voltage regulators that allow the board to be powered with anything from 3 to 16 volts. However using non-optimal voltage supply to the board limits the current that the board can supply. For example, supplied at 3.3 volts, the board can provide 500 mA of current. Supplied at 12 volts the board can only provide approximately 40 mA.2 For this reason, it was desirable to supply the board with 3.3 volts. Since the battery required by the actuator is 6 volts, a separate prototyping board is required to step the voltage down from 6 volts to 3.3 volts. This was accomplished using a LD1117 voltage regulator. A circuit diagram for wiring is available on the LD1117 data sheet available at http://goo.gl/gpr5jC (not included here for length reasons). This circuit was incorporated into the custom built prototyping board shown in Figure 17.

The signal required by the actuator is a 5 volt PWM signal, however the microcontroller produces a 3.3 volt PWM signal. In order to convert from 3.3 to 5 volts a logic level convert, part BOB-11978 available from https://www.sparkfun.com/products/11978 was used. This allows the logic to be stepped up from 3.3 to 5 volts. Full details on the implementation of the logic level converter can be found on the following website: https://www.sparkfun.com/products/11978. Using this chip requires a stable 5 volt input. For this, an L7800, 5 volt regulator was used and wired as shown in the component data sheet available at http://goo.gl/dlt2He (again, not included due to length). These components were incorporated into the custom built prototyping board shown in Figure 17.

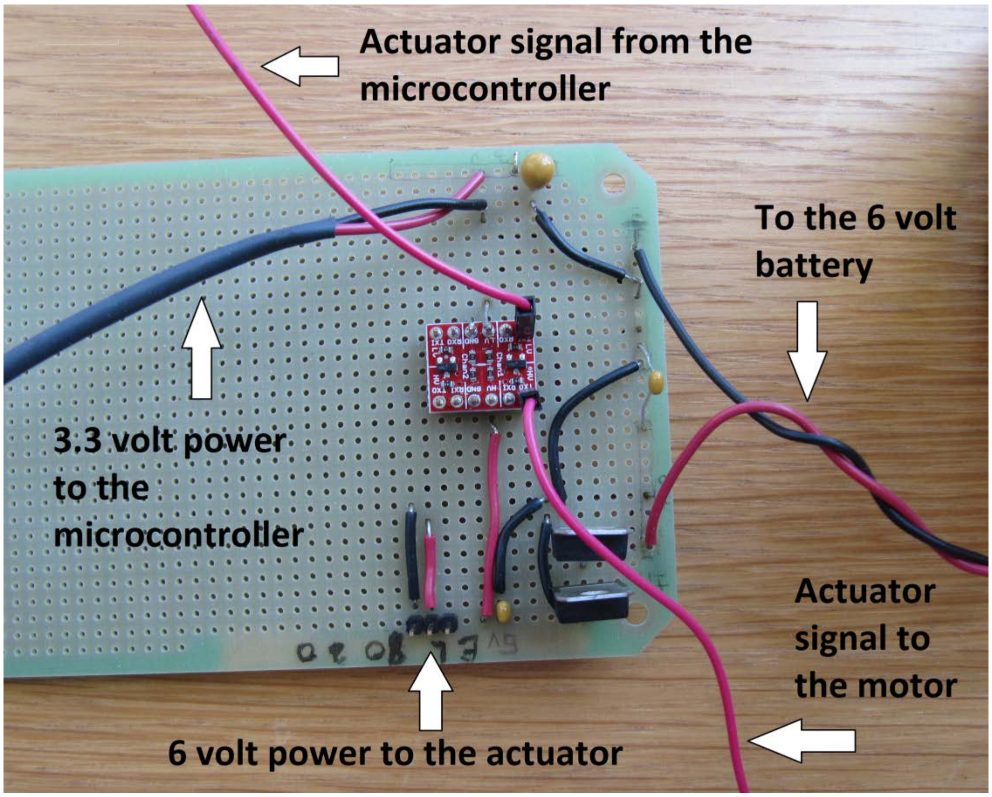

Figure 17: Prototyping board designed to provide all voltages needed for the microcontroller, actuator power and actuator signal.

The microcontroller was programmed using the custom Leaflabs Integrated Development Environment (IDE). The IDE can be downloaded and a full multi-library guide can be found at the following website: http://leaflabs.com/docs/maple-quickstart.html.

The original test program written for the microcontroller implemented two push buttons which, when pressed, would cause the actuator to either extend or retract fully. This was a test program and meant to be expanded on later. However a more complete program was never implemented due to a shift in the lab's experimental focus. The test code was produced by Tim Thomas, an intern in the lab. At the time of writing the test code, Tim had never previously written code, which is to say that a fully implemented code should be within reach of any researcher moderately familiar with programming.

The chosen programming environment is simple enough that an experimenter can chose what actions they wish to perform, modify existing sample codes provided with the IDE and then use that code in the microcontroller to perform their chosen experiments. With even rudimentary programming skills this should be easily accomplished in a time frame of minutes to hours.

C: Closing Remarks

The purpose of this research was to produce a high force magnetic tweezers device that was portable and would allow a range of new experiments to be done. The work done to optimize the force exerting capabilities of a magnet yoke array has shown that higher gradients cannot be achieved within the specification framework which motivated this research. Optimizing the B field gradient allowed the device to remain small meaning it can easily be used in conjunction with a number of imaging tools. The development of a platform for the accurate and reproducible positioning of the device will hopefully open up new possibilities for researchers who wish to study dynamic rheological or stress-strain behavior in a number of interesting and novel systems.

REFERENCES

1. F. Amblard, A. C. Maggs, B. Yurke, A. N. Pargellis and S. Leibler, Physical Review Letters **77** (21), 4470-4473 (1996).
2. K. C. Neuman and A. Nagy, Nature Methods **5** (6), 491-505 (2008).
3. J. Lin and M. T. Valentine, Review of Scientific Instruments **83** (5), 053905-053905-053905 (2012).
4. T. Strick, J.-F. Allemand, D. Bensimon, A. Bensimon and V. Croquette, Science **271** (5257), 1835-1837 (1996).
5. J. Zlatanova and S. H. Leuba, Biochemistry and Cell Biology **81** (3), 151-159 (2003).
6. C. Bustamante, Z. Bryant and S. B. Smith, Nature **421** (6921), 423-427 (2003).
7. I. De Vlaminck and C. Dekker, Annual Review of Biophysics **41**, 453-472 (2012).
8. Y. Yang, M. Bai, W. S. Klug, A. J. Levine and M. T. Valentine, Soft Matter **9** (2), 383-393 (2013).
9. A. R. Bausch, W. Möller and E. Sackmann, Biophysical Journal **76** (1), 573-579 (1999).
10. A. R. Bausch, F. Ziemann, A. A. Boulbitch, K. Jacobson and E. Sackmann, Biophysical Journal **75** (4), 2038-2049 (1998).
11. F. J. Alenghat, B. Fabry, K. Y. Tsai, W. H. Goldmann and D. E. Ingber, Biochemical and Biophysical Research Communications **277** (1), 93-99 (2000).
12. P. Kollmannsberger and B. Fabry, Review of Scientific Instruments **78** (11), 114301-114301-114306 (2007).
13. J. R. Moffitt, Y. R. Chemla, S. B. Smith and C. Bustamante, Annu. Rev. Biochem. **77**, 205-228 (2008).
14. Y. Yang, J. Lin, R. Meschewski, E. Watson and M. T. Valentine, BioTechniques **51** (1), 29-34 (2011).
15. A. H. de Vries, B. E. Krenn, R. van Driel and J. S. Kanger, Biophysical Journal **88** (3), 2137-2144 (2005).
16. C. Gosse and V. Croquette, Biophysical Journal **82** (6), 3314-3329 (2002).
17. J. Lipfert, X. Hao and N. H. Dekker, Biophysical Journal **96** (12), 5040-5049 (2009).
18. J. Lin and M. T. Valentine, Applied Physics Letters **100** (20), 201902 (2012).
19. D. C. Meeker, (2013).
20. D. Brown, B.-M. Ma and Z. Chen, Journal of Magnetism and Magnetic Materials **248** (3), 432-440 (2002).

Appendix A: Sample Matlab code for iterative FEA simulations

```
function FEMM_Master ()
% All lengths are in mm
RunName = 'Place_Name_here';    % give a name to your simulation run

        % Declare some variables that will help us track changes in
gradient and range
        % over the different iterations
        grad = 'Gradient ';
        work= 'Linear Working Range_(mm) ';
        ValuesNames = [grad, work];
        Values = [];
        set(0,'DefaultFigureVisible','off'); % This supresses Matlab
figures
        i = 0;

        mkdir('C:\Documents and Settings\Valentine\Desktop\AutoFEMM\',
RunName);
        cd(strcat('C:\Documents and
Settings\Valentine\Desktop\AutoFEMM\',RunName));
        RunDir = cd;
        mkdir('Meta'); %this is a meta folder that will have the data
for the whole run
        MetaDir = strcat(cd, '\', 'Meta');

MeshR = 10;  % Mesh refinement number creates a course mesh for
debugging
GOF = 0.95; % decide on a goodness of fit to check for the linear regime

for j = [0:1:5]; % j=[A,B,C] means j goes from A to C in steps of B
    % Add j to some parameter to iterate it (or iterate it in some other
    % way)

    i = i+1;        % This is the iteration number that will help name
the files

    % Write a new directory and make sure folder and file names are in
    % order
    cd(RunDir);
    stringi = sprintf('%03d' , i);                  % This is the string
version of the iteration number
    TestFolderName = strcat(RunName, stringi);      % This is the name
of the folder for a particular iteration
```

```
    mkdir(TestFolderName);                             % This makes the
folder named above
    DiskLocation = strcat(cd,'\',TestFolderName);   % This names the
folder we created
    cd (DiskLocation);                              % This puts us in
the folder we just created


OpenAndHide;  % this function opens FEMM and hides all of it's outputs
for speed

%% Build the Magnet
% Define Magnets

         LengthM = 25.3;          % length of margnets
         WidthM = 6.3;            % width of the magnets
         OffsetM = 6;             % distance between magnets
         RadM = 0.4;              % this is the fillet on the magnets

% Now create points that define the rectagle of our magnets

         M1x = LengthM/2;
         M1y = OffsetM;
         M2x = LengthM/2;
         M2y = OffsetM+WidthM;
         M3x = -LengthM/2;
         M3y = OffsetM+WidthM;
         M4x = -LengthM/2;
         M4y = OffsetM;

% Connect the dots to draw the magnets
mi_drawpolygon ([M1x,M1y;M2x,M2y;M3x,M3y;M4x,M4y])
mi_drawpolygon ([M1x,-M1y;M2x,-M2y;M3x,-M3y;M4x,-M4y])

% Now let's fillet all the corners

mi_createradius(M1x,M1y,RadM)
mi_createradius(M2x,M2y,RadM)
mi_createradius(M3x,M3y,RadM)
mi_createradius(M4x,M4y,RadM)
mi_createradius(M1x,-M1y,RadM)
mi_createradius(M2x,-M2y,RadM)
mi_createradius(M3x,-M3y,RadM)
mi_createradius(M4x,-M4y,RadM)


%%  Build the Yoke
%Define Geometry
     OffsetYT = 0.5;         % Distance between the yoke tips
     LengthYT = 2;           % Length of the yoke tip
     DistYT = 10;            % Distance from the edge of the magnet to
the yoke tip
     DepthY = 7+j;             % Depth to which the magnet fits into the
yoke
```

```
     ThkOutY = 5;            % Thickness of the outside face of the yoke
     ThkInY = 2;             % Thickness of the inside face of the yoke
     ArcStopOutY = 4;        % Distance from edge of magnet to beginning
of yoke arc on outside edge
     ArcStopInY = 4;         % Distance from edge of magnet to beginning
of yoke arc on inside edge
     AngleInY = 45;          % Angle of the inside curve from Y3 to Y4
     AngleOutY = 60;         % Angle of the outside curve from Y5 to Y6
     MaxSegY = 0.1;          % Max size of arc segments for the above
arcs
     PlotLength = 10;        % This is the length past the Yoke that we
will analyse


    %Define points
       Y1x = M1x - DepthY;
       Y1y = M1y;
       Y2x = M1x - DepthY;
       Y2y = M1y - ThkInY;
       Y3x = M1x + ArcStopInY;
       Y3y = M1y - ThkInY;
       Y4x = M1x + DistYT;
       Y4y = OffsetYT;
       Y5x = M1x + DistYT + LengthYT;
       Y5y = OffsetYT;
       Y6x = M1x + ArcStopOutY;
       Y6y = M2y + ThkOutY;
       Y7x = M1x - DepthY;
       Y7y = M2y + ThkOutY;
       Y8x = M1x - DepthY;
       Y8y = M2y;

    % Add all nodes
    mi_addnode(Y1x,Y1y)
    mi_addnode(Y2x,Y2y)
    mi_addnode(Y3x,Y3y)
    mi_addnode(Y4x,Y4y)
    mi_addnode(Y5x,Y5y)
    mi_addnode(Y6x,Y6y)
    mi_addnode(Y7x,Y7y)
    mi_addnode(Y8x,Y8y)

    mi_addnode(Y1x,-Y1y)
    mi_addnode(Y2x,-Y2y)
    mi_addnode(Y3x,-Y3y)
    mi_addnode(Y4x,-Y4y)
    mi_addnode(Y5x,-Y5y)
    mi_addnode(Y6x,-Y6y)
    mi_addnode(Y7x,-Y7y)
    mi_addnode(Y8x,-Y8y)


    % Draw all the straight lines first
```

```
        mi_addsegment(Y1x,Y1y, Y2x,Y2y)
        mi_addsegment(Y2x,Y2y, Y3x,Y3y)
        mi_addsegment(Y1x,-Y1y, Y2x,-Y2y)
        mi_addsegment(Y2x,-Y2y, Y3x,-Y3y)

        mi_addsegment(Y6x,Y6y, Y7x,Y7y)
        mi_addsegment(Y7x,Y7y, Y8x,Y8y)
        mi_addsegment(Y6x,-Y6y, Y7x,-Y7y)
        mi_addsegment(Y7x,-Y7y, Y8x,-Y8y)

        mi_addsegment(Y4x,Y4y, Y5x,Y5y)
        mi_addsegment(Y4x,-Y4y, Y5x,-Y5y)

    % Now draw all the curved segments
        %mi_addarc(x1,y1,x2,y2,angle,maxseg) Add an arc segment from
the node
        %(x1,y1) to node (x2,y2) with angle ‘angle’ divided into
‘maxseg’ segments.

        mi_addarc(Y4x,Y4y,Y3x,Y3y,AngleInY,MaxSegY)
        mi_addarc(Y3x,-Y3y,Y4x,-Y4y,AngleInY,MaxSegY)

        mi_addarc(Y5x,Y5y,Y6x,Y6y,AngleOutY,MaxSegY)
        mi_addarc(Y3x,-Y6y,Y5x,-Y5y,AngleOutY,MaxSegY)


%% Now define the Air geometry

        %Large air cirle
               RadA = 75;
               mi_addnode(0,RadA)
               mi_addnode(0,-RadA)
               mi_addarc(0,RadA,0,-RadA,180,0.5)
               mi_addarc(0,-RadA,0,RadA,180,0.5)

            %Small air area
               OverShootA = M1x + DistYT + LengthYT + 14;
               mi_addnode(OverShootA,Y6y)
               mi_addnode(OverShootA,-Y6y)
               mi_addsegment(Y2x,Y2y, Y2x,-Y2y)
               mi_addsegment(Y6x, Y6y, OverShootA,Y6y)
               mi_addsegment(Y6x, -Y6y, OverShootA,-Y6y)
               mi_addsegment(OverShootA,Y6y, OverShootA,-Y6y)

%%

% Populate the materials library

mi_getmaterial('Air')
mi_getmaterial('NdFeB 40 MGOe')
mi_getmaterial('1010 Steel')

% Define Blocks
```

```
    % Magnets
MeshSize1 = 0.5*MeshR;

B1x = 0;
B1y = ((M1y+M2y)/2);
mi_addblocklabel(B1x,B1y);
mi_seteditmode('blocks')
mi_selectlabel(B1x, B1y);
mi_setblockprop('NdFeB 40 MGOe', 0, MeshSize1, '', 0, 1,0);
mi_clearselected
mi_addblocklabel(B1x,-B1y)
mi_selectlabel(B1x, -B1y);
mi_setblockprop('NdFeB 40 MGOe', 0, MeshSize1, '', 180, 1,0);
mi_clearselected
    % Air
MeshSize2 = 1.2*MeshR;    % Large Bulk Air
B2x = 0;
B2y = RadA-2;
mi_addblocklabel(B2x,B2y);
mi_selectlabel(B2x, B2y);
mi_setblockprop('Air', 0, MeshSize2, '', 0, 2,0);
mi_clearselected

MeshSize3 = 0.1*MeshR;    % More refined mesh for the air around the
yoke tip
B3x = M1x;
B3y = 0;
mi_addblocklabel(B3x,B3y);
mi_selectlabel(B3x, B3y);
mi_setblockprop('Air', 0, MeshSize3, '', 0, 3,0);
mi_clearselected;

    % Yokes
MeshSize4 = 0.1*MeshR;
B4x = M1x + 2;
B4y = (M1y + M2y)/2;
mi_addblocklabel(B4x,B4y);
mi_addblocklabel(B4x,-B4y);
mi_selectlabel(B4x, B4y);
mi_selectlabel(B4x, -B4y);
mi_setblockprop('1010 Steel', 0, MeshSize4, '', 0, 4,0);
mi_clearselected

        % Add Boundary Conditions

        % Define the constants we need: Co = (1/(uo*RadA*mm)) ; C1 = 0
        Rtemp = RadA/1000;
        uo = 4*3.1415192654*(10^-7);
        ur = 1.00058986;
        Co = 1/(Rtemp*uo*ur);
        C1= 0;

        mi_addboundprop('Edge', 0, 0, 0, 0, 0, 0,  Co, C1, 2)
%Bdryformat = 2
```

```
        mi_seteditmode('arcsegments')
        mi_selectarcsegment(5, RadA-2) ;
        mi_selectarcsegment(-5, RadA-2) ;
        mi_setarcsegmentprop(5, 'Edge', 0, 5) ;
        mi_clearselected


% Save it and Mesh it!
filename = strcat(RunName, stringi);
mi_saveas(strcat(filename, '.fem'))
mi_purgemesh
mi_createmesh
mi_showmesh
mi_zoomnatural
mi_zoomin
mi_shownames()

        % Process and Post Processing
        mi_analyze();           % run the simulation
        mi_loadsolution ;       % load up the results
        mo_zoom(0,-20,50,20)    % Zoom: looking good
        mi_loadsolution ;       % have to reload it so that the zoom
works

% Now we set up the contour on which we look at the change in B field
    mo_seteditmode('contour')
    P1x = M1x + DistYT + LengthYT;      % contour starts where the yoke
ends
    P1y = 0;
    P2x = M1x + DistYT + LengthYT + PlotLength;
    P2y = 0;
    mo_addcontour(P1x,P1y)
    mo_addcontour(P2x,P2y)
    NamePot = 'Potential_A_';       % These create name strings that
will be used later to name files
    NameMagB = 'Magnitude_B_';
    mo_makeplot(0,500,strcat(NamePot,stringi,'.txt'),1)     % This saves
a text file with the values of magnetic potential and distance along the
contour
    mo_makeplot(1,500,strcat(NameMagB, stringi,'.txt'),1)   % This saves
a text file with the values of B field and distance along the contour

% Show the Density plot and safe it as a bitmap

upper_B = 1.4;
lower_B = 0;
mo_showdensityplot(1,0,upper_B,lower_B,'mag')       % This shows the
heat map of the magnetic field
mo_savebitmap(strcat ('Small_Density_Plot_',stringi,'.bmp')) % This
saves the file
BMP = imread(strcat ('Small_Density_Plot_',stringi,'.bmp'),'bmp');
    imwrite(BMP, strcat ('Small_Density_Plot_',stringi,'.jpeg'),'jpeg');
% delete(strcat ('Small_Density_Plot_',stringi,'.bmp'));
```

```
% mo_savemetafile('Large Density Plot.jpg') This file is about 3-5 MB,
only
% use if necessary
mo_close    % Closes post processor instance in order to prepare for the
next iteration
closefemm

%% Done with FEMM. Now plot and analyse the data

    % Plot the Potential along the x axis and save the file
[DistXA, Potential] = PlotA (NamePot, stringi);    %DistXA and Potential
are not strickly necessary
    % Plot the Magnitude of the B field along the x axis and save the
file
[DistXB, B ] = PlotB (NameMagB, stringi);


% Find the range over which the data is linear

Range = FindLinearRange(DistXB, B, GOF);
DistXB_Lin = DistXB(1:Range);   % These are the x values in the linear
regime
B_Lin = B(1:Range);             % These are the x values in the linear
regime

% Plot the Data with a Linear fit to the data and save it
name = 'B_field';
xlab2 = 'Dist';     % x label
ylab2 = 'B field';  % y label
PlotLinear (DistXB_Lin, B_Lin, name, xlab2, ylab2, stringi);
clf;
cab();

LinearRange = DistXB_Lin(Range);
LinEqu = [DistXB_Lin ones(Range,1)]\B_Lin;
Gradient = LinEqu(1);
Values(i,:) = [i Gradient LinearRange];


%% Done Plotting

cd(MetaDir);       % enter the Meta folder
WrMetaValues (Values);  % call the function to print the text file of
all relavent values

end

MetaPlot (Values, MetaDir, RunName);    % This function plots the Meta
data we have collected
CollectPlots(RunDir,RunName,i);         % This goes through every figure
iteration and collects them in the Meta folder
cd('C:\Documents and Settings\Valentine\Desktop\AutoFEMM\')
set(0,'DefaultFigureVisible','on'); % This turns Matlab figures back on
end
```

Appendix B: Dependence of $\nabla_{\mathbf{x}}|\vec{\mathbf{B}}|$ on each parameter with sample density plots

Dependence of $\nabla_x|\vec{B}|$ on parameter a: magnet offset

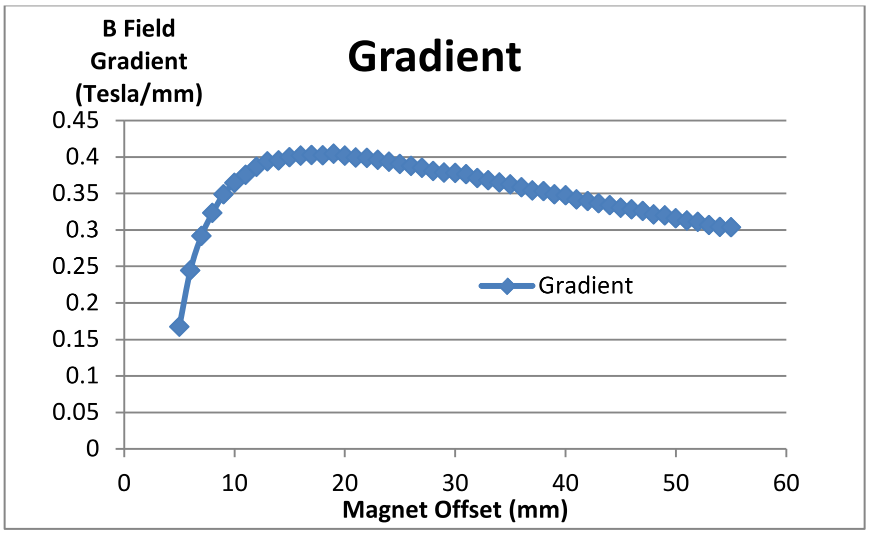

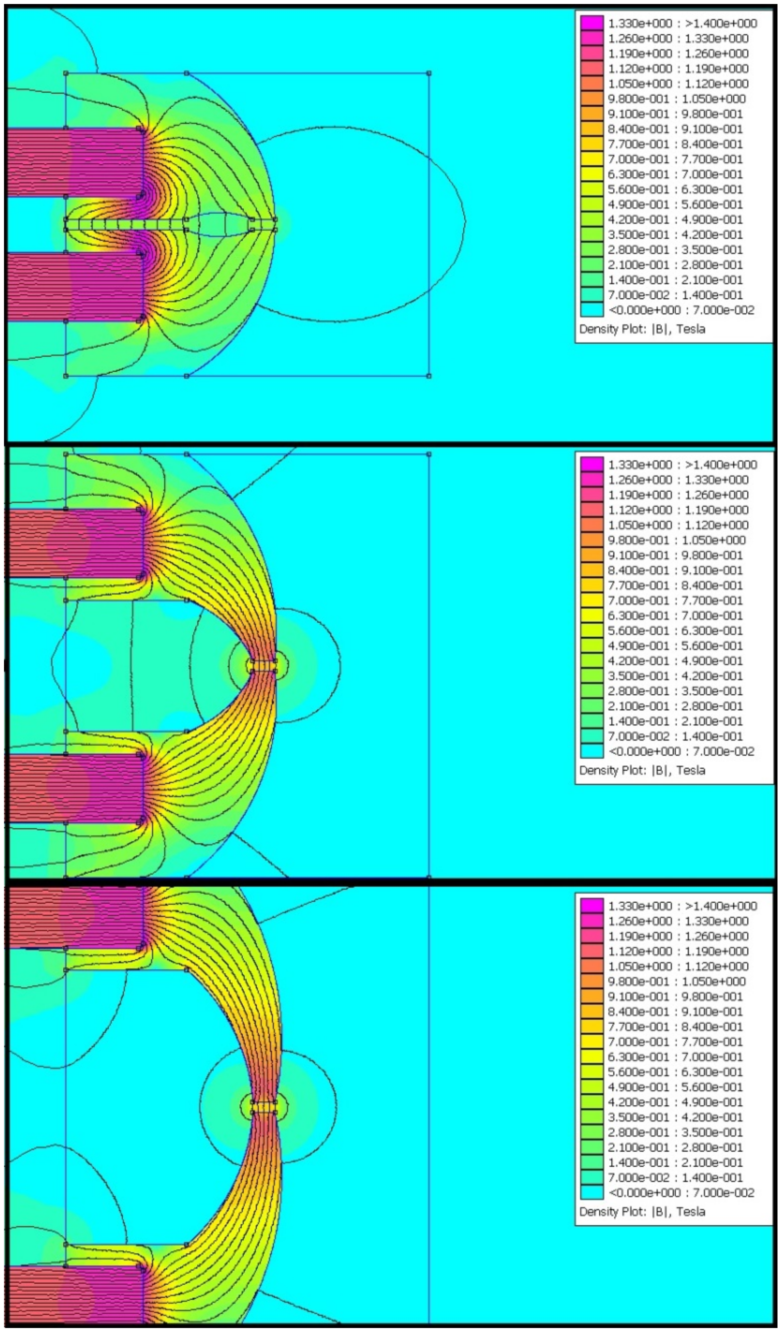
1.330e+000 : >1.400e+000
1.260e+000 : 1.330e+000
1.190e+000 : 1.260e+000
1.120e+000 : 1.190e+000
1.050e+000 : 1.120e+000
9.800e-001 : 1.050e+000
9.100e-001 : 9.800e-001
8.400e-001 : 9.100e-001
7.700e-001 : 8.400e-001
7.000e-001 : 7.700e-001
6.300e-001 : 7.000e-001
5.600e-001 : 6.300e-001
4.900e-001 : 5.600e-001
4.200e-001 : 4.900e-001
3.500e-001 : 4.200e-001
2.800e-001 : 3.500e-001
2.100e-001 : 2.800e-001
1.400e-001 : 2.100e-001
7.000e-002 : 1.400e-001
<0.000e+000 : 7.000e-002
Density Plot: |B|, Tesla
1.330e+000 : >1.400e+000
1.260e+000 : 1.330e+000
1.190e+000 : 1.260e+000
1.120e+000 : 1.190e+000
1.050e+000 : 1.120e+000
9.800e-001 : 1.050e+000
9.100e-001 : 9.800e-001
8.400e-001 : 9.100e-001
7.700e-001 : 8.400e-001
7.000e-001 : 7.700e-001
6.300e-001 : 7.000e-001
5.600e-001 : 6.300e-001
4.900e-001 : 5.600e-001
4.200e-001 : 4.900e-001
3.500e-001 : 4.200e-001
2.800e-001 : 3.500e-001
2.100e-001 : 2.800e-001
1.400e-001 : 2.100e-001
7.000e-002 : 1.400e-001
<0.000e+000 : 7.000e-002
Density Plot: |B|, Tesla
1.330e+000 : >1.400e+000
1.260e+000 : 1.330e+000
1.190e+000 : 1.260e+000
1.120e+000 : 1.190e+000
1.050e+000 : 1.120e+000
9.800e-001 : 1.050e+000
9.100e-001 : 9.800e-001
8.400e-001 : 9.100e-001
7.700e-001 : 8.400e-001
7.000e-001 : 7.700e-001
6.300e-001 : 7.000e-001
5.600e-001 : 6.300e-001
4.900e-001 : 5.600e-001
4.200e-001 : 4.900e-001
3.500e-001 : 4.200e-001
2.800e-001 : 3.500e-001
2.100e-001 : 2.800e-001
1.400e-001 : 2.100e-001
7.000e-002 : 1.400e-001
<0.000e+000 : 7.000e-002
Density Plot: |B|, Tesla

Dependence of $\nabla_x|\vec{B}|$ on parameter *b*: Inside yoke length. Note, this parameter is strongly coupled to *k*. The actual value used in the final design was tuned in conjunction with *k* and is not simply the maxima shown here.

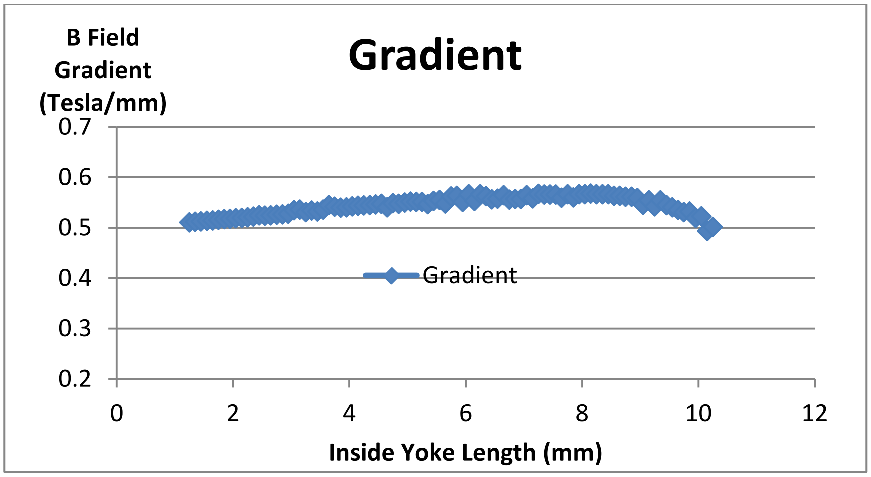

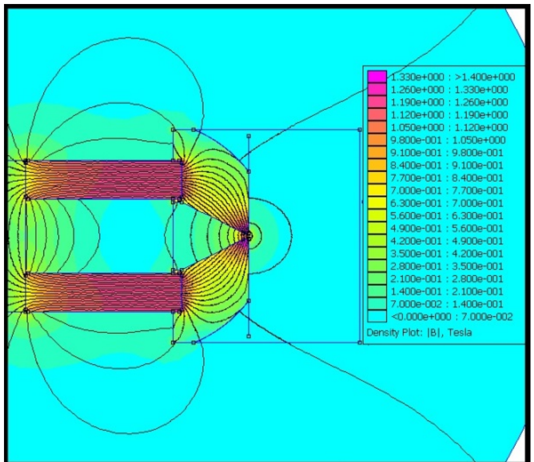
1.330e+000 : >1.400e+000
1.260e+000 : 1.330e+000
1.190e+000 : 1.260e+000
1.120e+000 : 1.190e+000
1.050e+000 : 1.120e+000
9.800e-001 : 1.050e+000
9.100e-001 : 9.800e-001
8.400e-001 : 9.100e-001
7.700e-001 : 8.400e-001
7.000e-001 : 7.700e-001
6.300e-001 : 7.000e-001
5.600e-001 : 6.300e-001
4.900e-001 : 5.600e-001
4.200e-001 : 4.900e-001
3.500e-001 : 4.200e-001
2.800e-001 : 3.500e-001
2.100e-001 : 2.800e-001
1.400e-001 : 2.100e-001
7.000e-002 : 1.400e-001
<0.000e+000 : 7.000e-002
Density Plot: |B|, Tesla

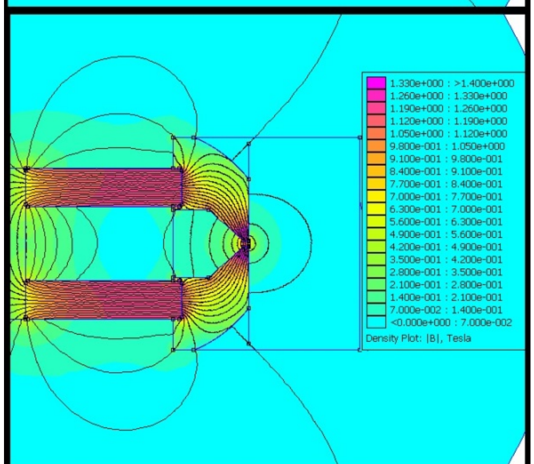
1.330e+000 : >1.400e+000
1.260e+000 : 1.330e+000
1.190e+000 : 1.260e+000
1.120e+000 : 1.190e+000
1.050e+000 : 1.120e+000
9.800e-001 : 1.050e+000
9.100e-001 : 9.800e-001
8.400e-001 : 9.100e-001
7.700e-001 : 8.400e-001
7.000e-001 : 7.700e-001
6.300e-001 : 7.000e-001
5.600e-001 : 6.300e-001
4.900e-001 : 5.600e-001
4.200e-001 : 4.900e-001
3.500e-001 : 4.200e-001
2.800e-001 : 3.500e-001
2.100e-001 : 2.800e-001
1.400e-001 : 2.100e-001
7.000e-002 : 1.400e-001
<0.000e+000 : 7.000e-002
Density Plot: |B|, Tesla

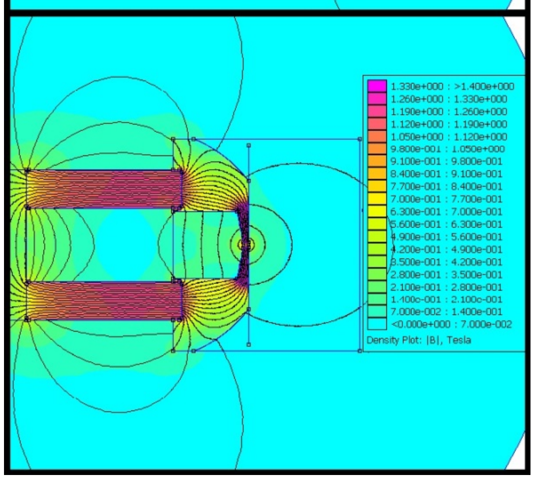
1.330e+000 : >1.400e+000
1.260e+000 : 1.330e+000
1.190e+000 : 1.260e+000
1.120e+000 : 1.190e+000
1.050e+000 : 1.120e+000
9.800e-001 : 1.050e+000
9.100e-001 : 9.800e-001
8.400e-001 : 9.100e-001
7.700e-001 : 8.400e-001
7.000e-001 : 7.700e-001
6.300e-001 : 7.000e-001
5.600e-001 : 6.300e-001
4.900e-001 : 5.600e-001
4.200e-001 : 4.900e-001
3.500e-001 : 4.200e-001
2.800e-001 : 3.500e-001
2.100e-001 : 2.800e-001
1.400e-001 : 2.100e-001
7.000e-002 : 1.400e-001
<0.000e+000 : 7.000e-002
Density Plot: |B|, Tesla

Dependence of $\nabla_x|\vec{B}|$ on parameter c: Yoke tip length

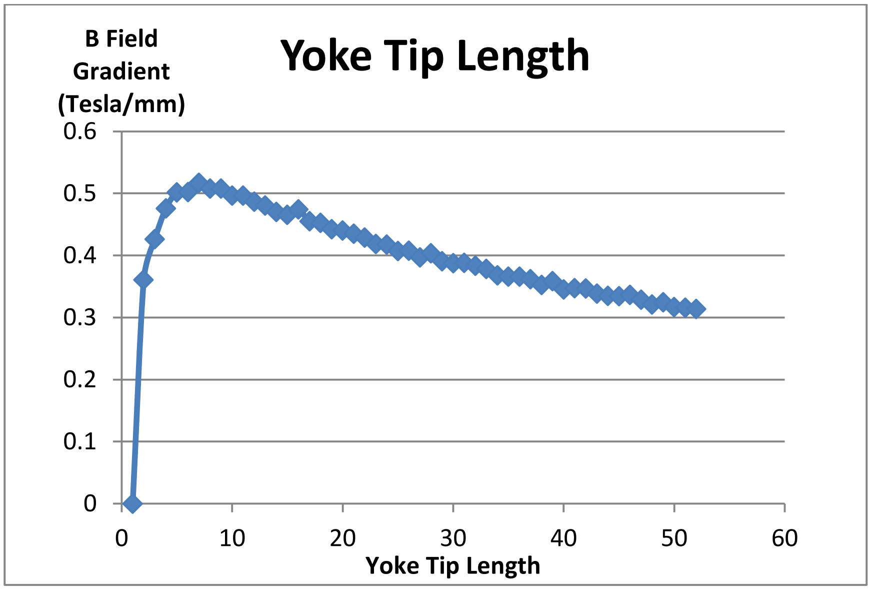

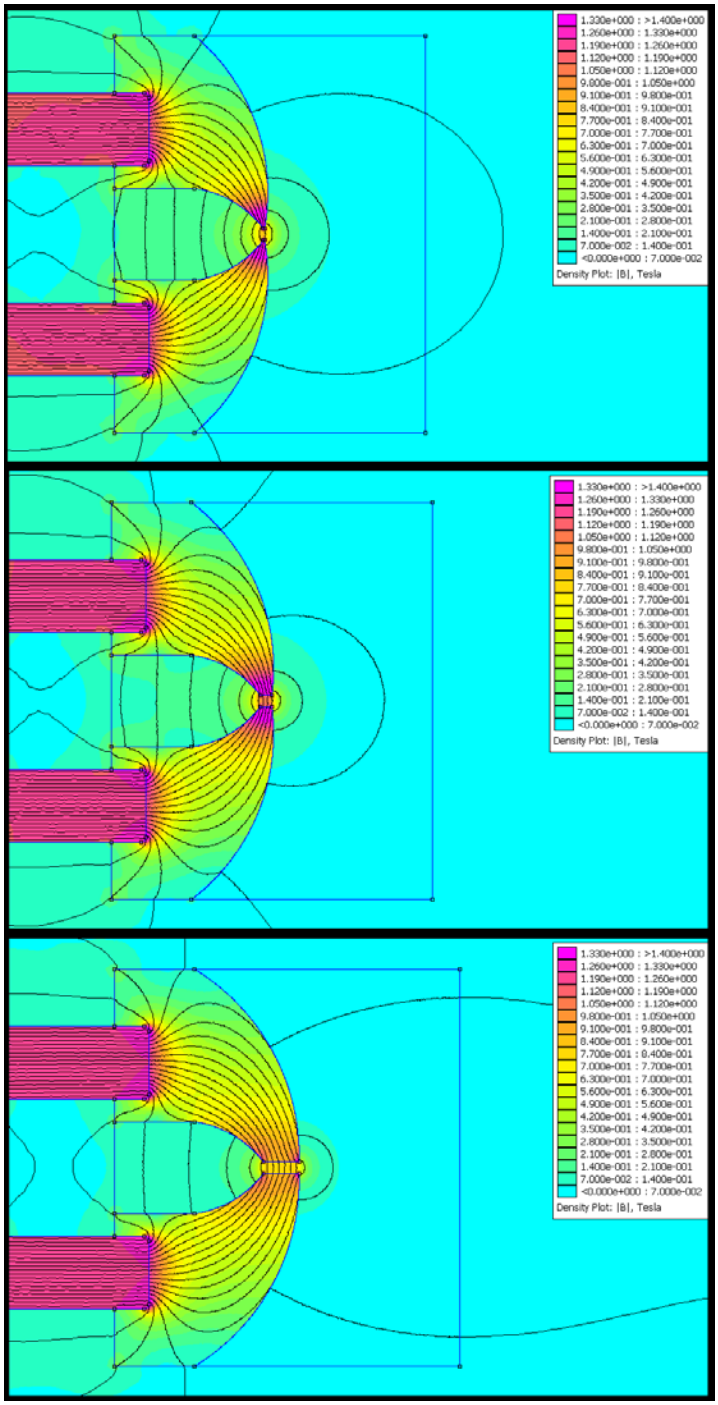
1.330e+000 : >1.400e+000
1.260e+000 : 1.330e+000
1.190e+000 : 1.260e+000
1.120e+000 : 1.190e+000
1.050e+000 : 1.120e+000
9.800e-001 : 1.050e+000
9.100e-001 : 9.800e-001
8.400e-001 : 9.100e-001
7.700e-001 : 8.400e-001
7.000e-001 : 7.700e-001
6.300e-001 : 7.000e-001
5.600e-001 : 6.300e-001
4.900e-001 : 5.600e-001
4.200e-001 : 4.900e-001
3.500e-001 : 4.200e-001
2.800e-001 : 3.500e-001
2.100e-001 : 2.800e-001
1.400e-001 : 2.100e-001
7.000e-002 : 1.400e-001
<0.000e+000 : 7.000e-002
Density Plot: |B|, Tesla
1.330e+000 : >1.400e+000
1.260e+000 : 1.330e+000
1.190e+000 : 1.260e+000
1.120e+000 : 1.190e+000
1.050e+000 : 1.120e+000
9.800e-001 : 1.050e+000
9.100e-001 : 9.800e-001
8.400e-001 : 9.100e-001
7.700e-001 : 8.400e-001
7.000e-001 : 7.700e-001
6.300e-001 : 7.000e-001
5.600e-001 : 6.300e-001
4.900e-001 : 5.600e-001
4.200e-001 : 4.900e-001
3.500e-001 : 4.200e-001
2.800e-001 : 3.500e-001
2.100e-001 : 2.800e-001
1.400e-001 : 2.100e-001
7.000e-002 : 1.400e-001
<0.000e+000 : 7.000e-002
Density Plot: |B|, Tesla
1.330e+000 : >1.400e+000
1.260e+000 : 1.330e+000
1.190e+000 : 1.260e+000
1.120e+000 : 1.190e+000
1.050e+000 : 1.120e+000
9.800e-001 : 1.050e+000
9.100e-001 : 9.800e-001
8.400e-001 : 9.100e-001
7.700e-001 : 8.400e-001
7.000e-001 : 7.700e-001
6.300e-001 : 7.000e-001
5.600e-001 : 6.300e-001
4.900e-001 : 5.600e-001
4.200e-001 : 4.900e-001
3.500e-001 : 4.200e-001
2.800e-001 : 3.500e-001
2.100e-001 : 2.800e-001
1.400e-001 : 2.100e-001
7.000e-002 : 1.400e-001
<0.000e+000 : 7.000e-002
Density Plot: |B|, Tesla

Dependence of $\nabla_x|\vec{B}|$ on parameter *d*: Depth of yoke cut (see main body of text: Results - 1. Finite Element Analysis).

Dependence of $\nabla_x|\vec{B}|$ on parameter *e*: Magnet Length

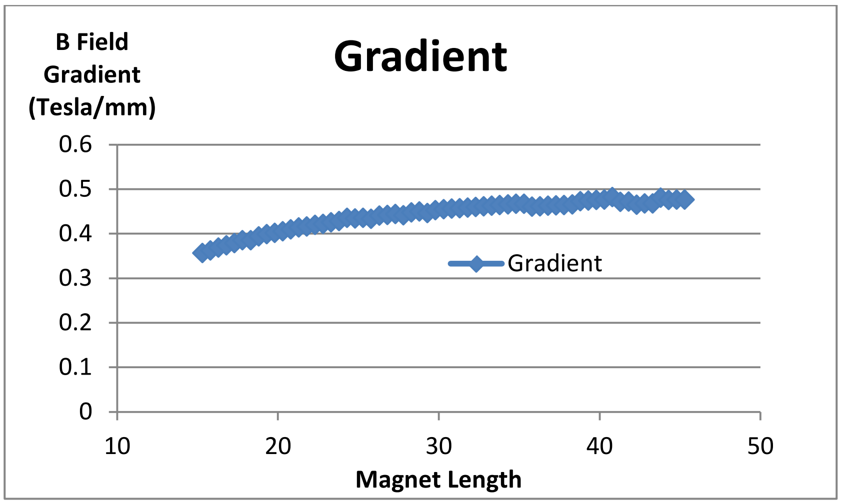

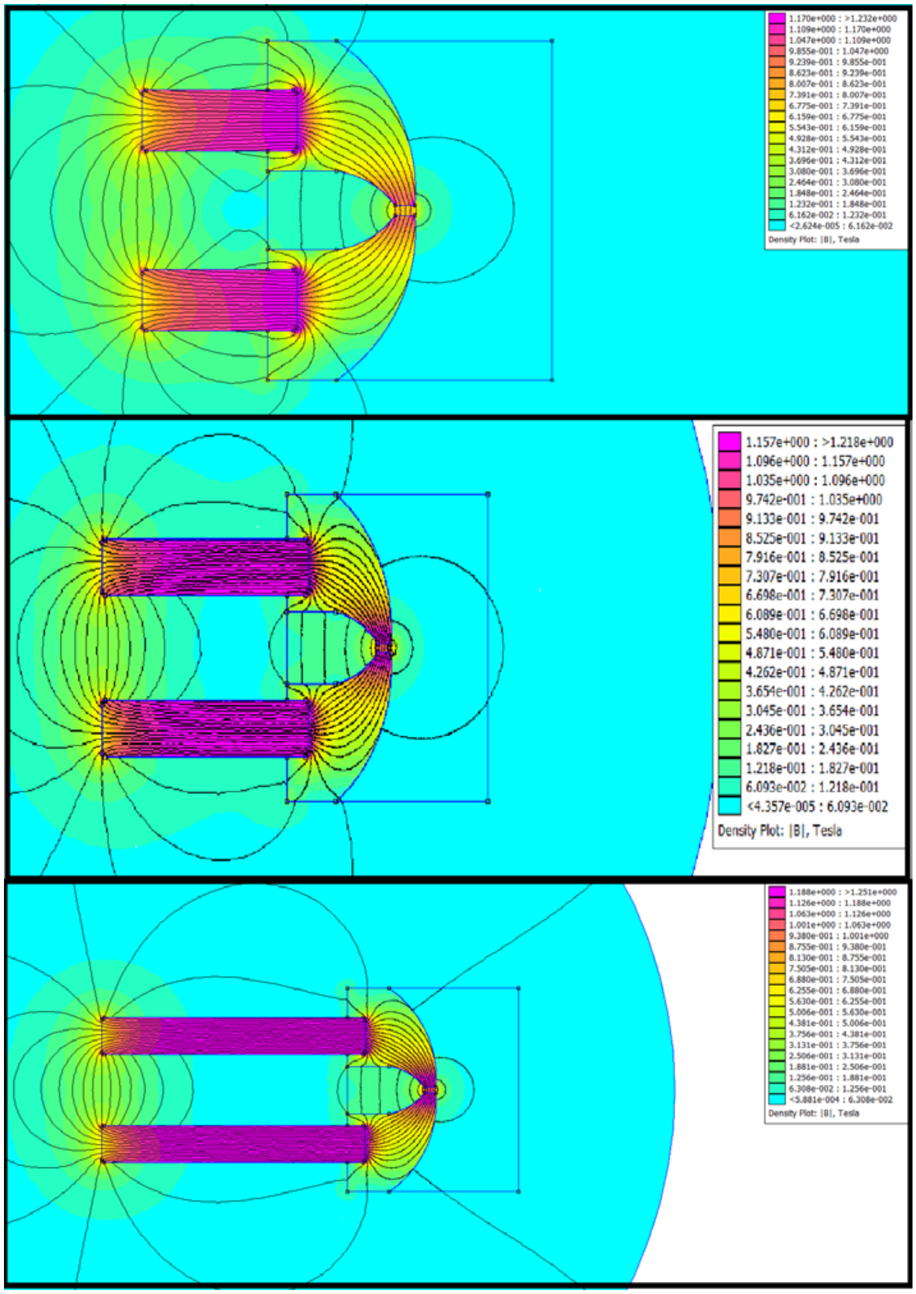
1.170e+000 : >1.232e+000
1.109e+000 : 1.170e+000
1.047e+000 : 1.109e+000
9.855e-001 : 1.047e+000
9.239e-001 : 9.855e-001
8.623e-001 : 9.239e-001
8.007e-001 : 8.623e-001
7.391e-001 : 8.007e-001
6.775e-001 : 7.391e-001
6.159e-001 : 6.775e-001
5.543e-001 : 6.159e-001
4.928e-001 : 5.543e-001
4.312e-001 : 4.928e-001
3.696e-001 : 4.312e-001
3.080e-001 : 3.696e-001
2.464e-001 : 3.080e-001
1.848e-001 : 2.464e-001
1.232e-001 : 1.848e-001
6.162e-002 : 1.232e-001
<2.624e-005 : 6.162e-002
Density Plot: |B|, Tesla
1.157e+000 : >1.218e+000
1.096e+000 : 1.157e+000
1.035e+000 : 1.096e+000
9.742e-001 : 1.035e+000
9.133e-001 : 9.742e-001
8.525e-001 : 9.133e-001
7.916e-001 : 8.525e-001
7.307e-001 : 7.916e-001
6.698e-001 : 7.307e-001
6.089e-001 : 6.698e-001
5.480e-001 : 6.089e-001
4.871e-001 : 5.480e-001
4.262e-001 : 4.871e-001
3.654e-001 : 4.262e-001
3.045e-001 : 3.654e-001
2.436e-001 : 3.045e-001
1.827e-001 : 2.436e-001
1.218e-001 : 1.827e-001
6.093e-002 : 1.218e-001
<4.357e-005 : 6.093e-002
Density Plot: |B|, Tesla
1.188e+000 : >1.251e+000
1.126e+000 : 1.188e+000
1.063e+000 : 1.126e+000
1.001e+000 : 1.063e+000
9.380e-001 : 1.001e+000
8.755e-001 : 9.380e-001
8.130e-001 : 8.755e-001
7.505e-001 : 8.130e-001
6.880e-001 : 7.505e-001
6.255e-001 : 6.880e-001
5.630e-001 : 6.255e-001
5.006e-001 : 5.630e-001
4.381e-001 : 5.006e-001
3.756e-001 : 4.381e-001
3.131e-001 : 3.756e-001
2.506e-001 : 3.131e-001
1.881e-001 : 2.506e-001
1.256e-001 : 1.881e-001
6.308e-002 : 1.256e-001
<5.881e-004 : 6.308e-002
Density Plot: |B|, Tesla

Dependence of $\nabla_x|\vec{B}|$ on parameter *f*: Magnet Width

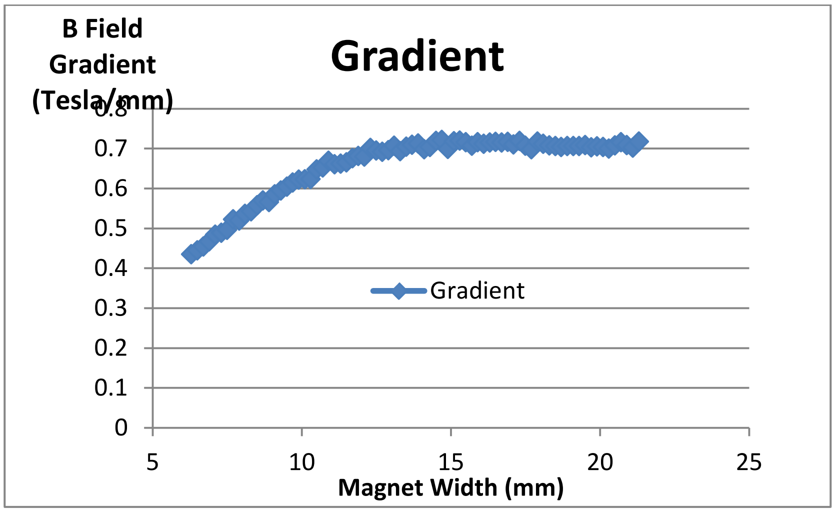

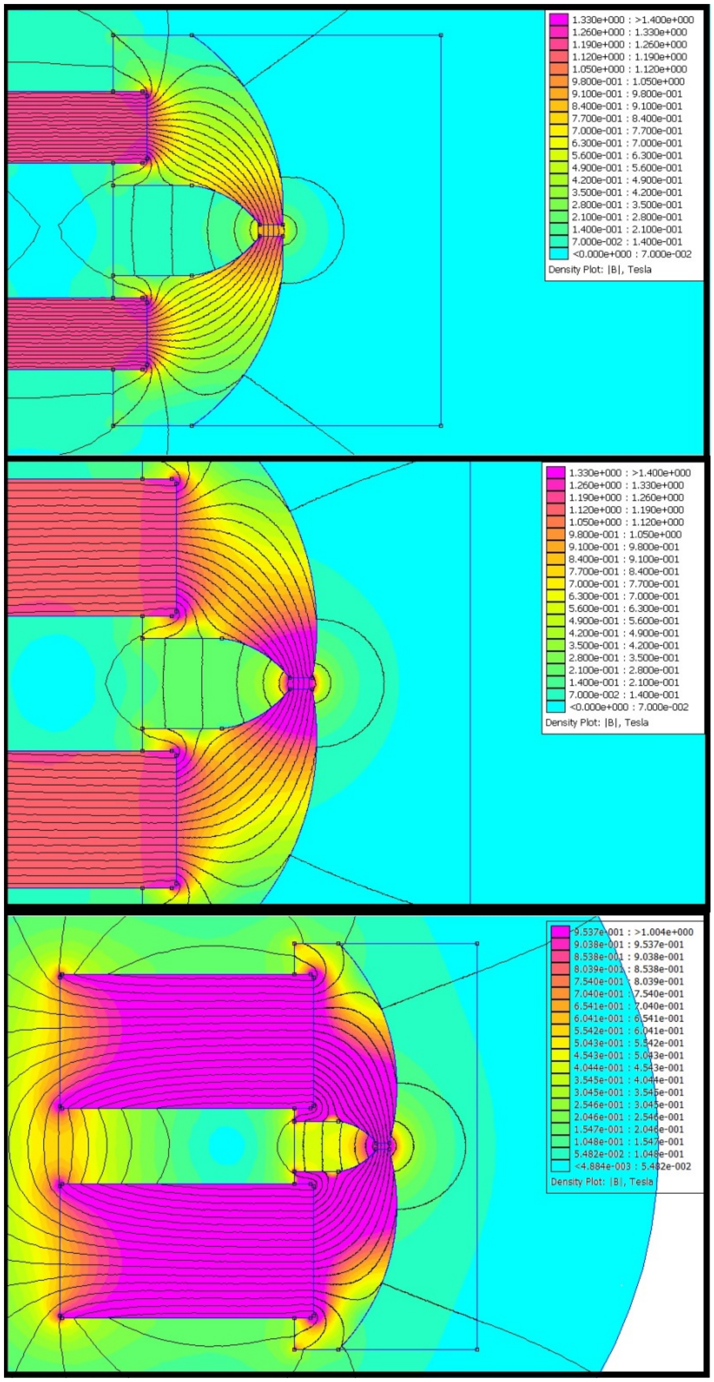
1.330e+000 : >1.400e+000
1.260e+000 : 1.330e+000
1.190e+000 : 1.260e+000
1.120e+000 : 1.190e+000
1.050e+000 : 1.120e+000
9.800e-001 : 1.050e+000
9.100e-001 : 9.800e-001
8.400e-001 : 9.100e-001
7.700e-001 : 8.400e-001
7.000e-001 : 7.700e-001
6.300e-001 : 7.000e-001
5.600e-001 : 6.300e-001
4.900e-001 : 5.600e-001
4.200e-001 : 4.900e-001
3.500e-001 : 4.200e-001
2.800e-001 : 3.500e-001
2.100e-001 : 2.800e-001
1.400e-001 : 2.100e-001
7.000e-002 : 1.400e-001
<0.000e+000 : 7.000e-002
Density Plot: |B|, Tesla
1.330e+000 : >1.400e+000
1.260e+000 : 1.330e+000
1.190e+000 : 1.260e+000
1.120e+000 : 1.190e+000
1.050e+000 : 1.120e+000
9.800e-001 : 1.050e+000
9.100e-001 : 9.800e-001
8.400e-001 : 9.100e-001
7.700e-001 : 8.400e-001
7.000e-001 : 7.700e-001
6.300e-001 : 7.000e-001
5.600e-001 : 6.300e-001
4.900e-001 : 5.600e-001
4.200e-001 : 4.900e-001
3.500e-001 : 4.200e-001
2.800e-001 : 3.500e-001
2.100e-001 : 2.800e-001
1.400e-001 : 2.100e-001
7.000e-002 : 1.400e-001
<0.000e+000 : 7.000e-002
Density Plot: |B|, Tesla
9.537e-001 : >1.004e+000
9.038e-001 : 9.537e-001
8.538e-001 : 9.038e-001
8.039e-001 : 8.538e-001
7.540e-001 : 8.039e-001
7.040e-001 : 7.540e-001
6.541e-001 : 7.040e-001
6.041e-001 : 6.541e-001
5.542e-001 : 6.041e-001
5.043e-001 : 5.542e-001
4.543e-001 : 5.043e-001
4.044e-001 : 4.543e-001
3.545e-001 : 4.044e-001
3.045e-001 : 3.545e-001
2.546e-001 : 3.045e-001
2.046e-001 : 2.546e-001
1.547e-001 : 2.046e-001
1.048e-001 : 1.547e-001
5.482e-002 : 1.048e-001
<4.884e-003 : 5.482e-002
Density Plot: |B|, Tesla

Dependence of $\nabla_x \left|\vec{B}\right|$ on parameter g: Inner yoke angle

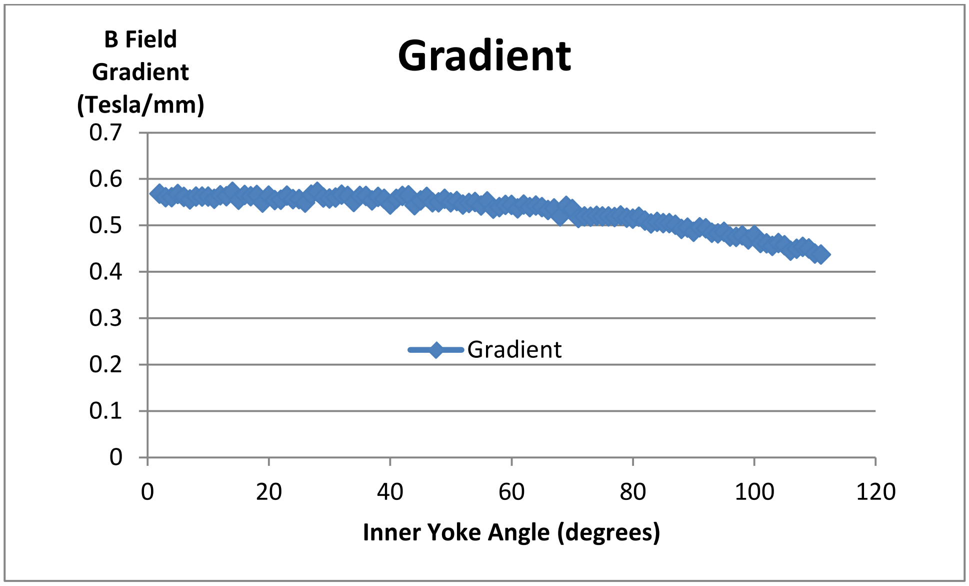

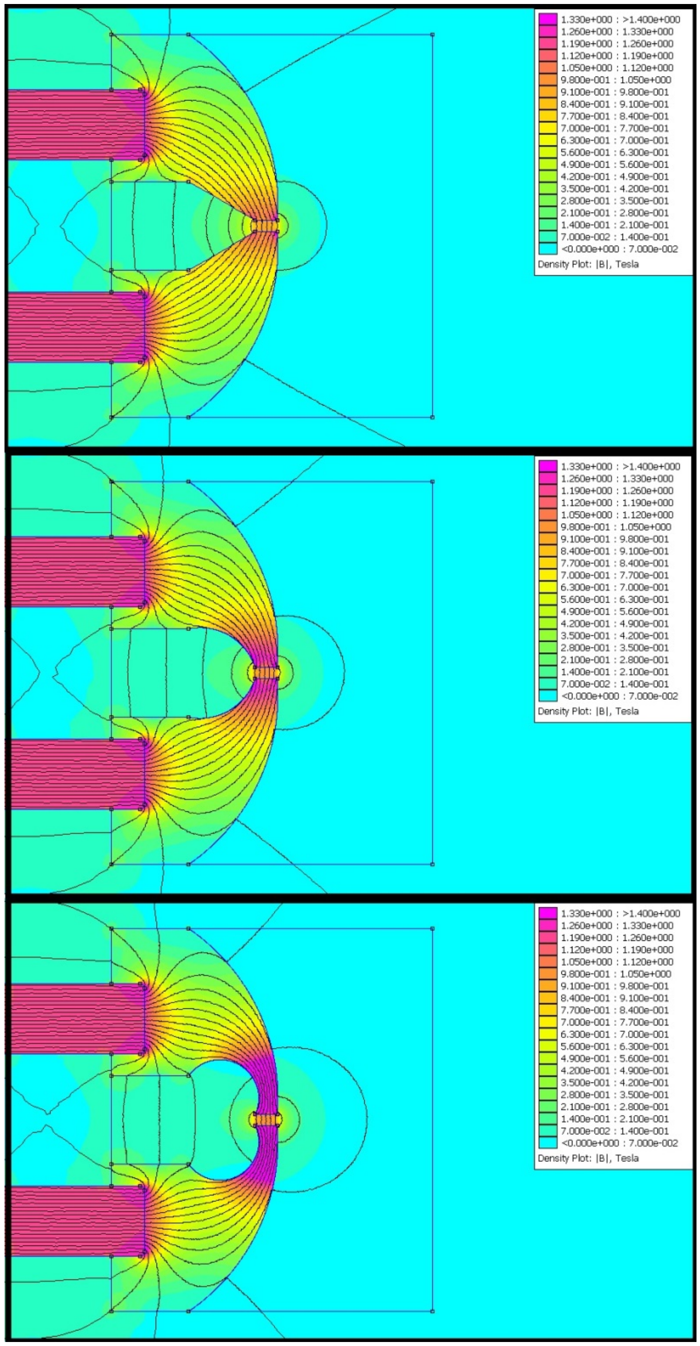
1.330e+000 : >1.400e+000
1.260e+000 : 1.330e+000
1.190e+000 : 1.260e+000
1.120e+000 : 1.190e+000
1.050e+000 : 1.120e+000
9.800e-001 : 1.050e+000
9.100e-001 : 9.800e-001
8.400e-001 : 9.100e-001
7.700e-001 : 8.400e-001
7.000e-001 : 7.700e-001
6.300e-001 : 7.000e-001
5.600e-001 : 6.300e-001
4.900e-001 : 5.600e-001
4.200e-001 : 4.900e-001
3.500e-001 : 4.200e-001
2.800e-001 : 3.500e-001
2.100e-001 : 2.800e-001
1.400e-001 : 2.100e-001
7.000e-002 : 1.400e-001
<0.000e+000 : 7.000e-002
Density Plot: |B|, Tesla

Dependence of $\nabla_x|\vec{B}|$ on parameter h: Outside yoke thickness

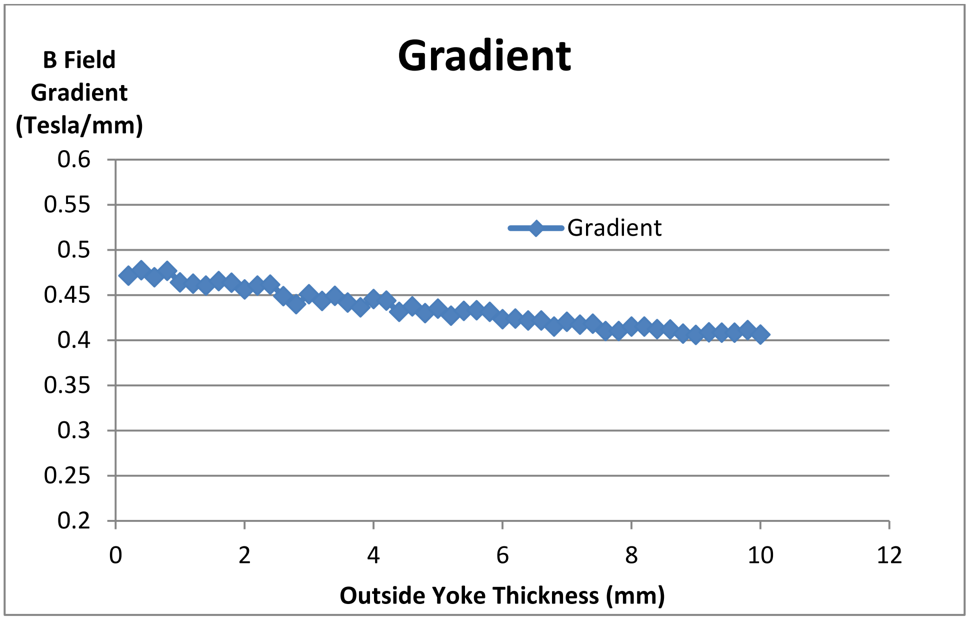

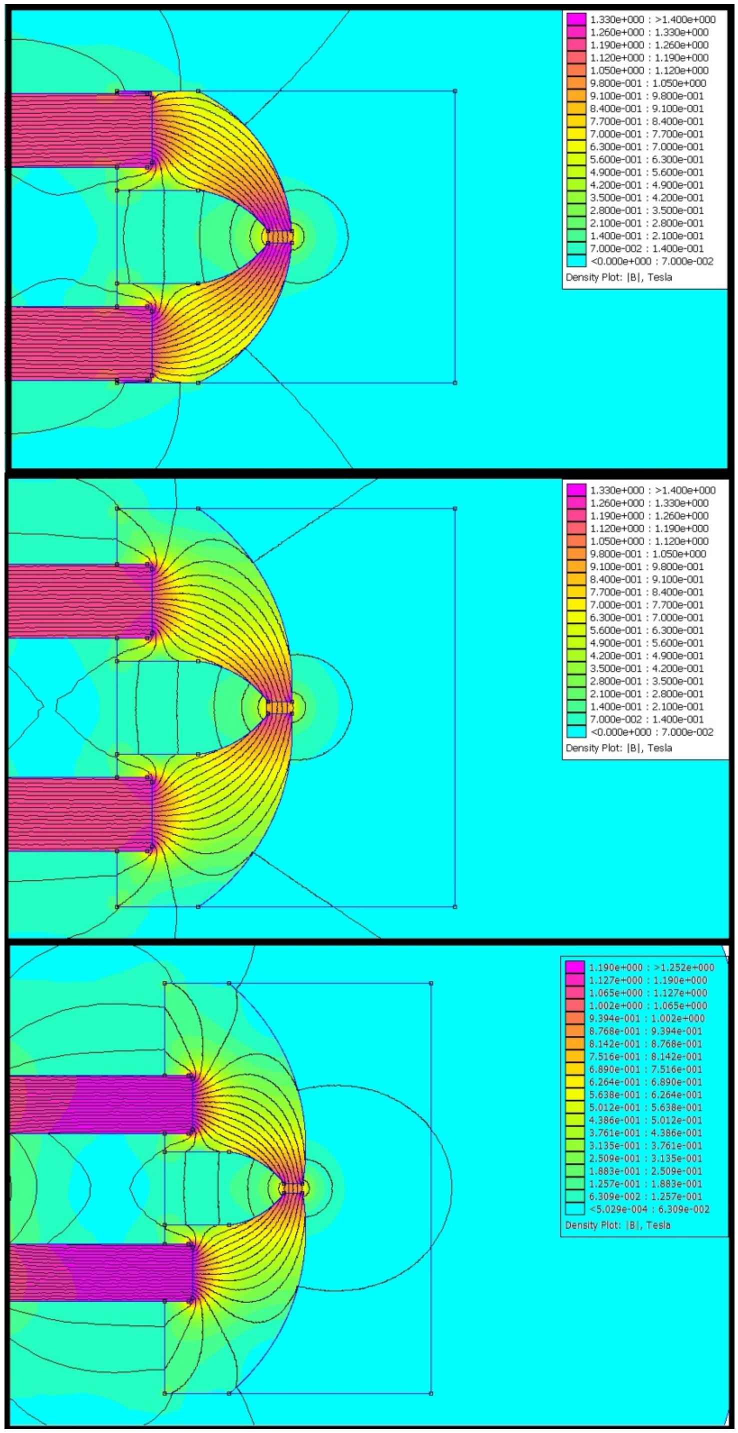
1.330e+000 : >1.400e+000
1.260e+000 : 1.330e+000
1.190e+000 : 1.260e+000
1.120e+000 : 1.190e+000
1.050e+000 : 1.120e+000
9.800e-001 : 1.050e+000
9.100e-001 : 9.800e-001
8.400e-001 : 9.100e-001
7.700e-001 : 8.400e-001
7.000e-001 : 7.700e-001
6.300e-001 : 7.000e-001
5.600e-001 : 6.300e-001
4.900e-001 : 5.600e-001
4.200e-001 : 4.900e-001
3.500e-001 : 4.200e-001
2.800e-001 : 3.500e-001
2.100e-001 : 2.800e-001
1.400e-001 : 2.100e-001
7.000e-002 : 1.400e-001
<0.000e+000 : 7.000e-002
Density Plot: |B|, Tesla
1.330e+000 : >1.400e+000
1.260e+000 : 1.330e+000
1.190e+000 : 1.260e+000
1.120e+000 : 1.190e+000
1.050e+000 : 1.120e+000
9.800e-001 : 1.050e+000
9.100e-001 : 9.800e-001
8.400e-001 : 9.100e-001
7.700e-001 : 8.400e-001
7.000e-001 : 7.700e-001
6.300e-001 : 7.000e-001
5.600e-001 : 6.300e-001
4.900e-001 : 5.600e-001
4.200e-001 : 4.900e-001
3.500e-001 : 4.200e-001
2.800e-001 : 3.500e-001
2.100e-001 : 2.800e-001
1.400e-001 : 2.100e-001
7.000e-002 : 1.400e-001
<0.000e+000 : 7.000e-002
Density Plot: |B|, Tesla
1.190e+000 : >1.252e+000
1.127e+000 : 1.190e+000
1.065e+000 : 1.127e+000
1.002e+000 : 1.065e+000
9.394e-001 : 1.002e+000
8.768e-001 : 9.394e-001
8.142e-001 : 8.768e-001
7.516e-001 : 8.142e-001
6.890e-001 : 7.516e-001
6.264e-001 : 6.890e-001
5.638e-001 : 6.264e-001
5.012e-001 : 5.638e-001
4.386e-001 : 5.012e-001
3.761e-001 : 4.386e-001
3.135e-001 : 3.761e-001
2.509e-001 : 3.135e-001
1.883e-001 : 2.509e-001
1.257e-001 : 1.883e-001
6.309e-002 : 1.257e-001
<5.029e-004 : 6.309e-002
Density Plot: |B|, Tesla

Dependence of $\nabla_x|\vec{B}|$ on parameter i: Inside yoke thickness

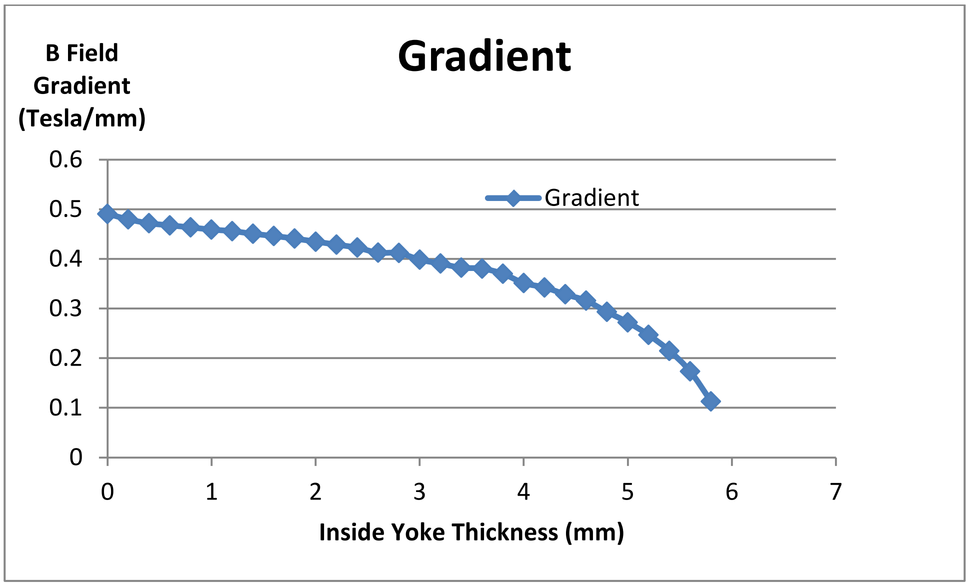

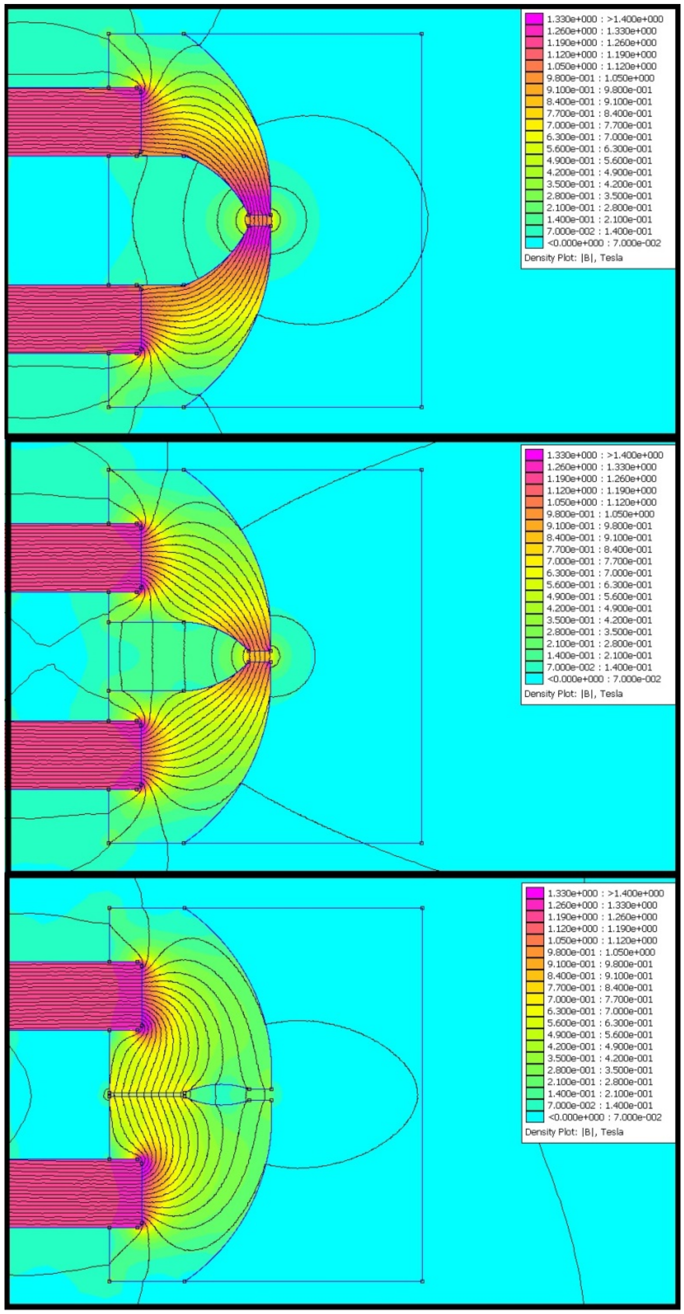
1.330e+000 : >1.400e+000
1.260e+000 : 1.330e+000
1.190e+000 : 1.260e+000
1.120e+000 : 1.190e+000
1.050e+000 : 1.120e+000
9.800e-001 : 1.050e+000
9.100e-001 : 9.800e-001
8.400e-001 : 9.100e-001
7.700e-001 : 8.400e-001
7.000e-001 : 7.700e-001
6.300e-001 : 7.000e-001
5.600e-001 : 6.300e-001
4.900e-001 : 5.600e-001
4.200e-001 : 4.900e-001
3.500e-001 : 4.200e-001
2.800e-001 : 3.500e-001
2.100e-001 : 2.800e-001
1.400e-001 : 2.100e-001
7.000e-002 : 1.400e-001
<0.000e+000 : 7.000e-002
Density Plot: |B|, Tesla

Dependence of $\nabla_x|\vec{B}|$ on parameter j: Yoke depth (see main body of text: Results - 1. Finite Element Analysis).

Dependence of $\nabla_x|\vec{B}|$ on parameter k: Distance to yoke tip

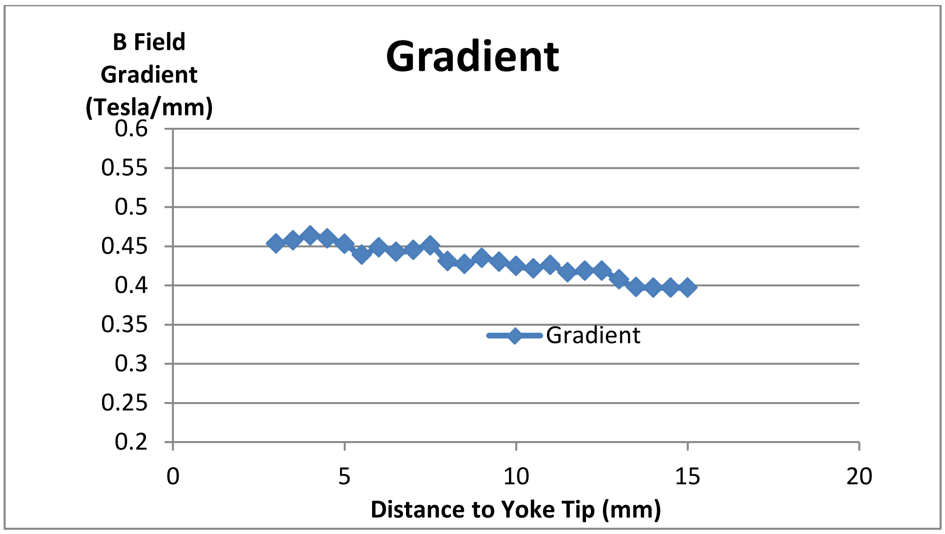

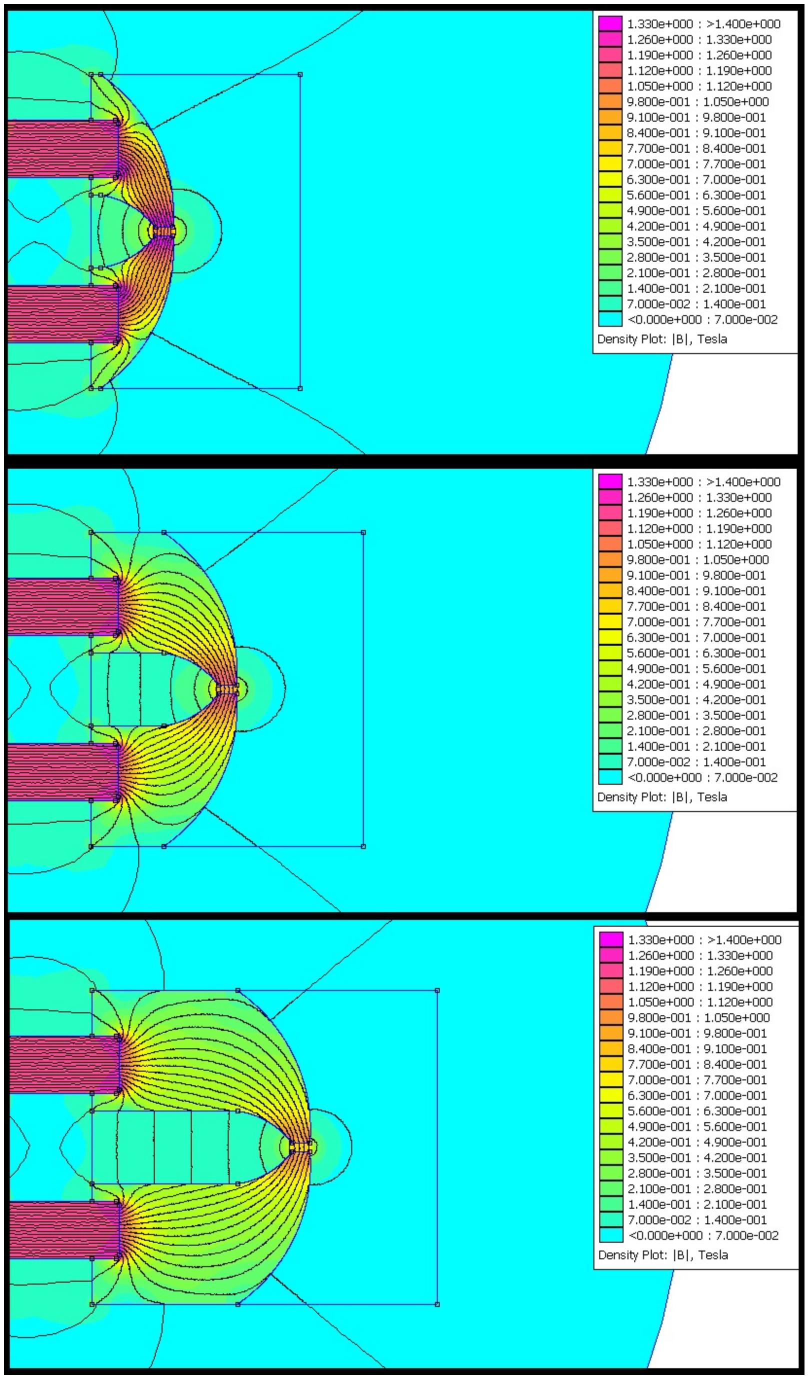
1.330e+000 : >1.400e+000
1.260e+000 : 1.330e+000
1.190e+000 : 1.260e+000
1.120e+000 : 1.190e+000
1.050e+000 : 1.120e+000
9.800e-001 : 1.050e+000
9.100e-001 : 9.800e-001
8.400e-001 : 9.100e-001
7.700e-001 : 8.400e-001
7.000e-001 : 7.700e-001
6.300e-001 : 7.000e-001
5.600e-001 : 6.300e-001
4.900e-001 : 5.600e-001
4.200e-001 : 4.900e-001
3.500e-001 : 4.200e-001
2.800e-001 : 3.500e-001
2.100e-001 : 2.800e-001
1.400e-001 : 2.100e-001
7.000e-002 : 1.400e-001
<0.000e+000 : 7.000e-002
Density Plot: |B|, Tesla
1.330e+000 : >1.400e+000
1.260e+000 : 1.330e+000
1.190e+000 : 1.260e+000
1.120e+000 : 1.190e+000
1.050e+000 : 1.120e+000
9.800e-001 : 1.050e+000
9.100e-001 : 9.800e-001
8.400e-001 : 9.100e-001
7.700e-001 : 8.400e-001
7.000e-001 : 7.700e-001
6.300e-001 : 7.000e-001
5.600e-001 : 6.300e-001
4.900e-001 : 5.600e-001
4.200e-001 : 4.900e-001
3.500e-001 : 4.200e-001
2.800e-001 : 3.500e-001
2.100e-001 : 2.800e-001
1.400e-001 : 2.100e-001
7.000e-002 : 1.400e-001
<0.000e+000 : 7.000e-002
Density Plot: |B|, Tesla
1.330e+000 : >1.400e+000
1.260e+000 : 1.330e+000
1.190e+000 : 1.260e+000
1.120e+000 : 1.190e+000
1.050e+000 : 1.120e+000
9.800e-001 : 1.050e+000
9.100e-001 : 9.800e-001
8.400e-001 : 9.100e-001
7.700e-001 : 8.400e-001
7.000e-001 : 7.700e-001
6.300e-001 : 7.000e-001
5.600e-001 : 6.300e-001
4.900e-001 : 5.600e-001
4.200e-001 : 4.900e-001
3.500e-001 : 4.200e-001
2.800e-001 : 3.500e-001
2.100e-001 : 2.800e-001
1.400e-001 : 2.100e-001
7.000e-002 : 1.400e-001
<0.000e+000 : 7.000e-002
Density Plot: |B|, Tesla

Dependence of $\nabla_x|\vec{B}|$ on parameter l: Outer Yoke Angle

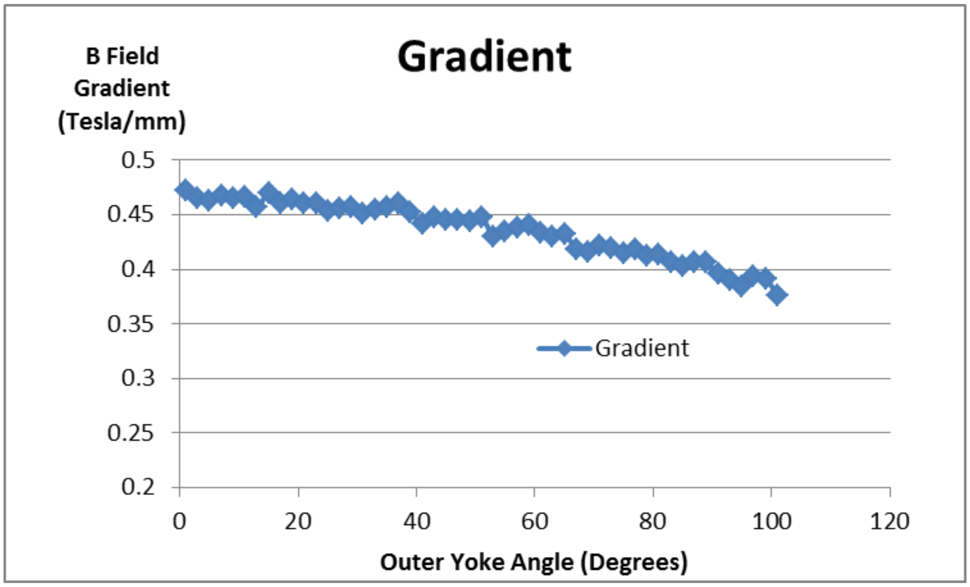

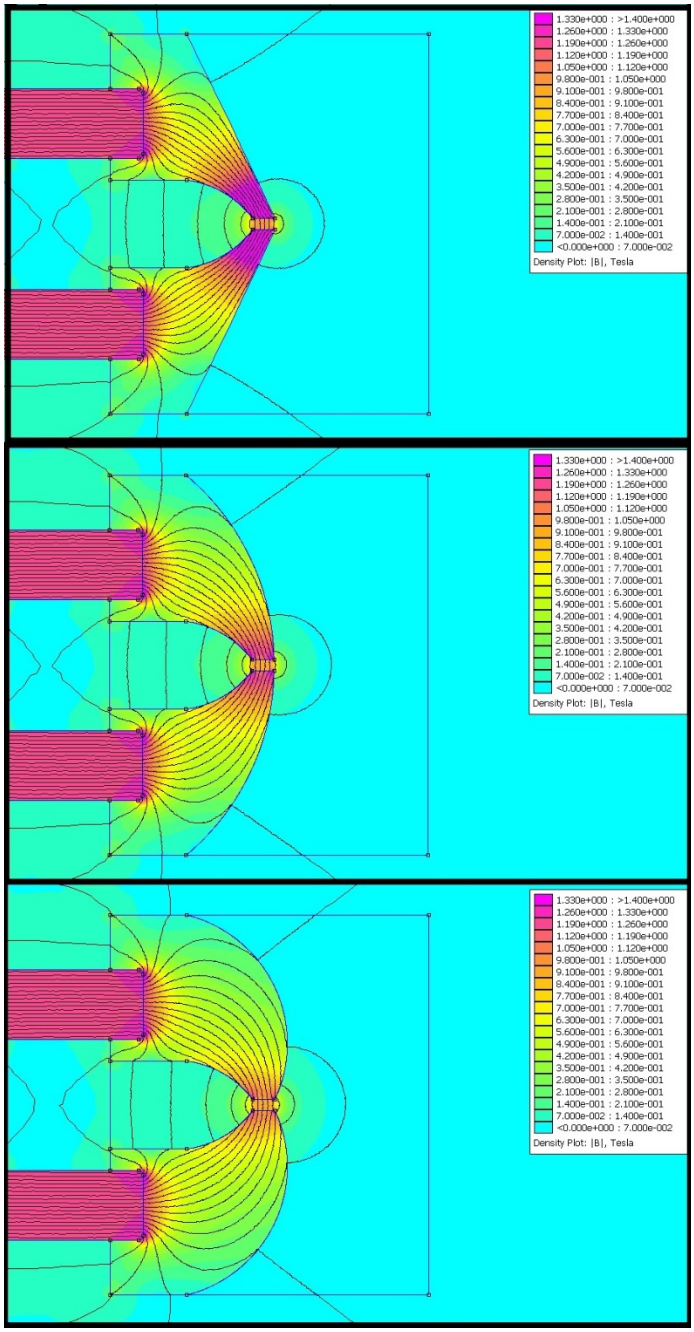
1.330e+000 : >1.400e+000
1.260e+000 : 1.330e+000
1.190e+000 : 1.260e+000
1.120e+000 : 1.190e+000
1.050e+000 : 1.120e+000
9.800e-001 : 1.050e+000
9.100e-001 : 9.800e-001
8.400e-001 : 9.100e-001
7.700e-001 : 8.400e-001
7.000e-001 : 7.700e-001
6.300e-001 : 7.000e-001
5.600e-001 : 6.300e-001
4.900e-001 : 5.600e-001
4.200e-001 : 4.900e-001
3.500e-001 : 4.200e-001
2.800e-001 : 3.500e-001
2.100e-001 : 2.800e-001
1.400e-001 : 2.100e-001
7.000e-002 : 1.400e-001
<0.000e+000 : 7.000e-002
Density Plot: |B|, Tesla
1.330e+000 : >1.400e+000
1.260e+000 : 1.330e+000
1.190e+000 : 1.260e+000
1.120e+000 : 1.190e+000
1.050e+000 : 1.120e+000
9.800e-001 : 1.050e+000
9.100e-001 : 9.800e-001
8.400e-001 : 9.100e-001
7.700e-001 : 8.400e-001
7.000e-001 : 7.700e-001
6.300e-001 : 7.000e-001
5.600e-001 : 6.300e-001
4.900e-001 : 5.600e-001
4.200e-001 : 4.900e-001
3.500e-001 : 4.200e-001
2.800e-001 : 3.500e-001
2.100e-001 : 2.800e-001
1.400e-001 : 2.100e-001
7.000e-002 : 1.400e-001
<0.000e+000 : 7.000e-002
Density Plot: |B|, Tesla
1.330e+000 : >1.400e+000
1.260e+000 : 1.330e+000
1.190e+000 : 1.260e+000
1.120e+000 : 1.190e+000
1.050e+000 : 1.120e+000
9.800e-001 : 1.050e+000
9.100e-001 : 9.800e-001
8.400e-001 : 9.100e-001
7.700e-001 : 8.400e-001
7.000e-001 : 7.700e-001
6.300e-001 : 7.000e-001
5.600e-001 : 6.300e-001
4.900e-001 : 5.600e-001
4.200e-001 : 4.900e-001
3.500e-001 : 4.200e-001
2.800e-001 : 3.500e-001
2.100e-001 : 2.800e-001
1.400e-001 : 2.100e-001
7.000e-002 : 1.400e-001
<0.000e+000 : 7.000e-002
Density Plot: |B|, Tesla

Dependence of $\nabla_x|\vec{B}|$ on parameter m: Tip Separation

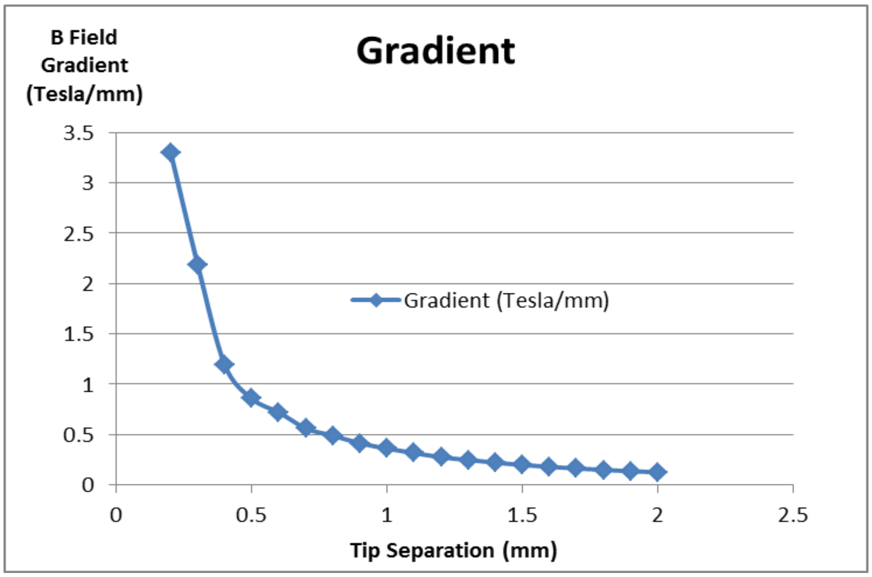

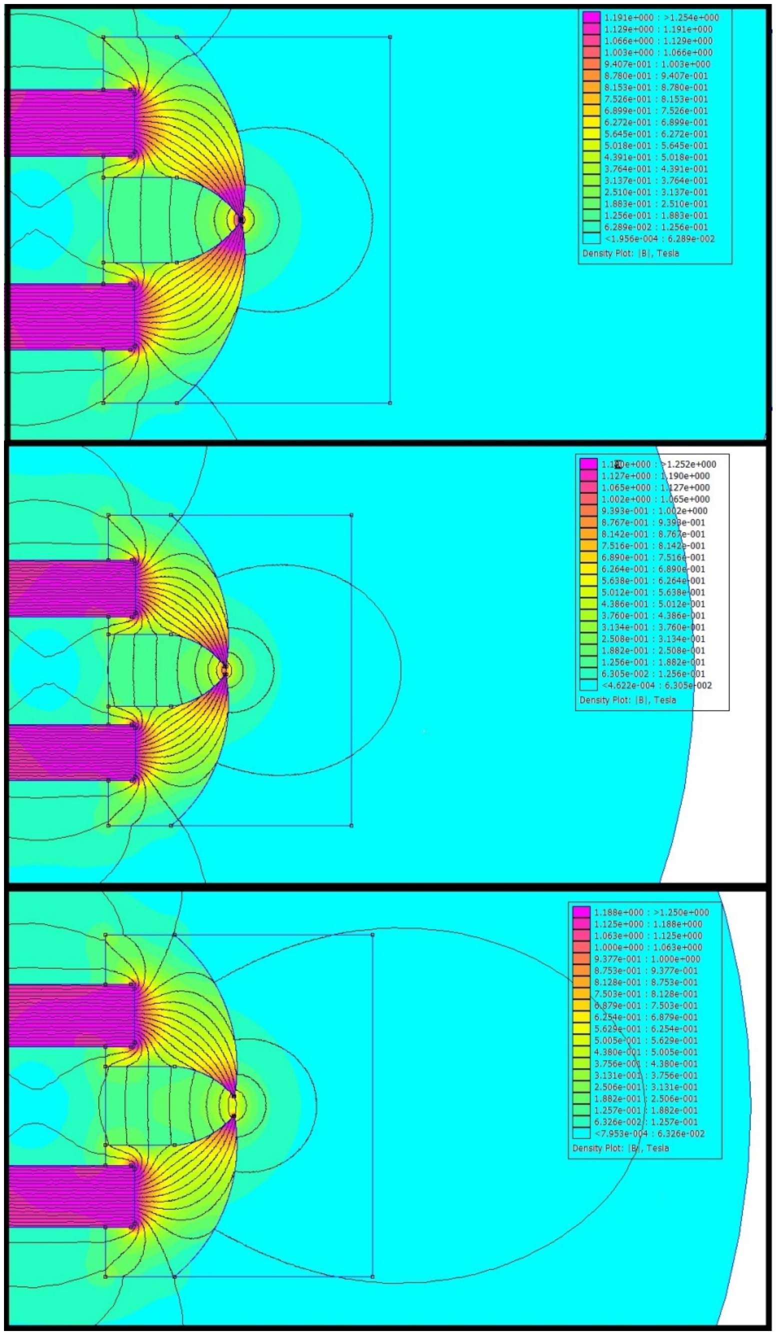
1.191e+000 : >1.254e+000
1.129e+000 : 1.191e+000
1.066e+000 : 1.129e+000
1.003e+000 : 1.066e+000
9.407e-001 : 1.003e+000
8.780e-001 : 9.407e-001
8.153e-001 : 8.780e-001
7.526e-001 : 8.153e-001
6.899e-001 : 7.526e-001
6.272e-001 : 6.899e-001
5.645e-001 : 6.272e-001
5.018e-001 : 5.645e-001
4.391e-001 : 5.018e-001
3.764e-001 : 4.391e-001
3.137e-001 : 3.764e-001
2.510e-001 : 3.137e-001
1.883e-001 : 2.510e-001
1.256e-001 : 1.883e-001
6.289e-002 : 1.256e-001
<1.956e-004 : 6.289e-002
Density Plot: |B|, Tesla
1.127e+000 : 1.190e+000
1.065e+000 : 1.127e+000
1.002e+000 : 1.065e+000
9.393e-001 : 1.002e+000
8.767e-001 : 9.393e-001
8.142e-001 : 8.767e-001
7.516e-001 : 8.142e-001
6.890e-001 : 7.516e-001
6.264e-001 : 6.890e-001
5.638e-001 : 6.264e-001
5.012e-001 : 5.638e-001
4.386e-001 : 5.012e-001
3.760e-001 : 4.386e-001
3.134e-001 : 3.760e-001
2.508e-001 : 3.134e-001
1.882e-001 : 2.508e-001
1.256e-001 : 1.882e-001
6.305e-002 : 1.256e-001
<4.622e-004 : 6.305e-002
Density Plot: |B|, Tesla
1.188e+000 : >1.250e+000
1.125e+000 : 1.188e+000
1.063e+000 : 1.125e+000
1.000e+000 : 1.063e+000
9.377e-001 : 1.000e+000
8.753e-001 : 9.377e-001
8.128e-001 : 8.753e-001
7.503e-001 : 8.128e-001
6.879e-001 : 7.503e-001
6.254e-001 : 6.879e-001
5.629e-001 : 6.254e-001
5.005e-001 : 5.629e-001
4.380e-001 : 5.005e-001
3.756e-001 : 4.380e-001
3.131e-001 : 3.756e-001
2.506e-001 : 3.131e-001
1.882e-001 : 2.506e-001
1.257e-001 : 1.882e-001
6.326e-002 : 1.257e-001
<7.953e-004 : 6.326e-002
Density Plot: |B|, Tesla

Dependence of $\nabla_x|\vec{B}|$ on parameter *n*: Magnet edge radius

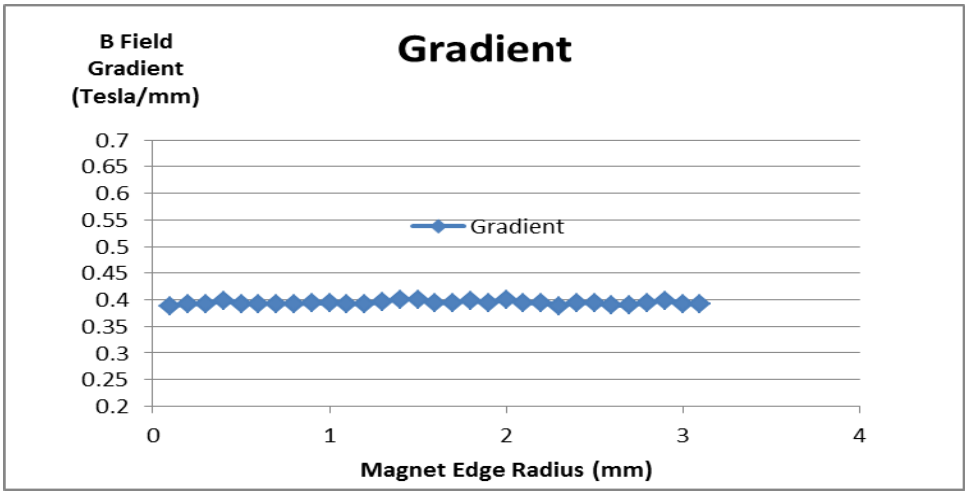

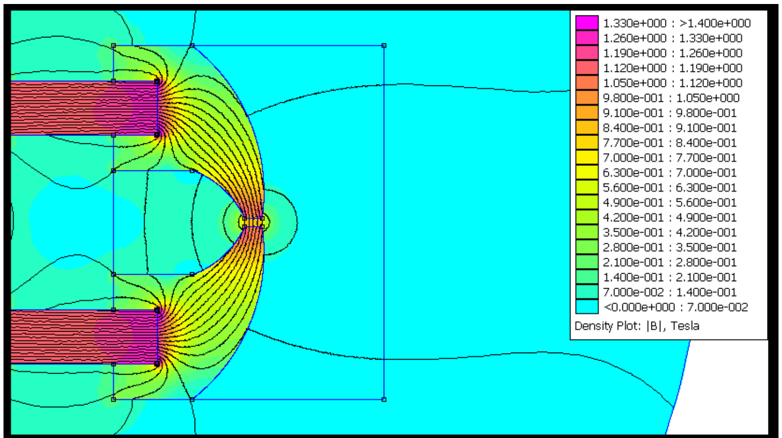
1.330e+000 : >1.400e+000
1.260e+000 : 1.330e+000
1.190e+000 : 1.260e+000
1.120e+000 : 1.190e+000
1.050e+000 : 1.120e+000
9.800e-001 : 1.050e+000
9.100e-001 : 9.800e-001
8.400e-001 : 9.100e-001
7.700e-001 : 8.400e-001
7.000e-001 : 7.700e-001
6.300e-001 : 7.000e-001
5.600e-001 : 6.300e-001
4.900e-001 : 5.600e-001
4.200e-001 : 4.900e-001
3.500e-001 : 4.200e-001
2.800e-001 : 3.500e-001
2.100e-001 : 2.800e-001
1.400e-001 : 2.100e-001
7.000e-002 : 1.400e-001
<0.000e+000 : 7.000e-002
Density Plot: |B|, Tesla

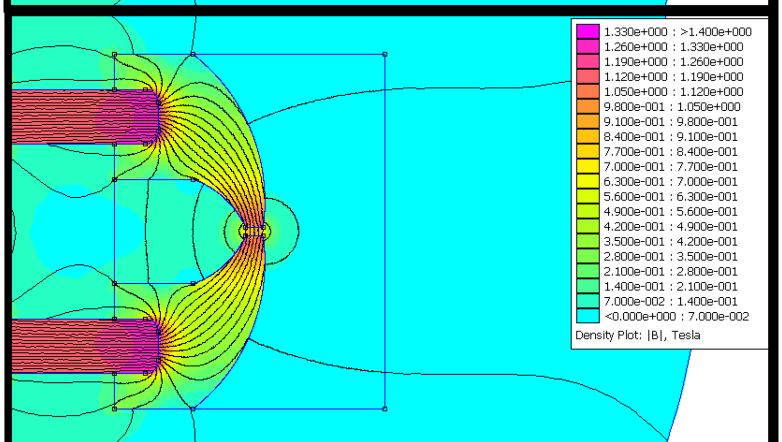
1.330e+000 : >1.400e+000
1.260e+000 : 1.330e+000
1.190e+000 : 1.260e+000
1.120e+000 : 1.190e+000
1.050e+000 : 1.120e+000
9.800e-001 : 1.050e+000
9.100e-001 : 9.800e-001
8.400e-001 : 9.100e-001
7.700e-001 : 8.400e-001
7.000e-001 : 7.700e-001
6.300e-001 : 7.000e-001
5.600e-001 : 6.300e-001
4.900e-001 : 5.600e-001
4.200e-001 : 4.900e-001
3.500e-001 : 4.200e-001
2.800e-001 : 3.500e-001
2.100e-001 : 2.800e-001
1.400e-001 : 2.100e-001
7.000e-002 : 1.400e-001
<0.000e+000 : 7.000e-002
Density Plot: |B|, Tesla

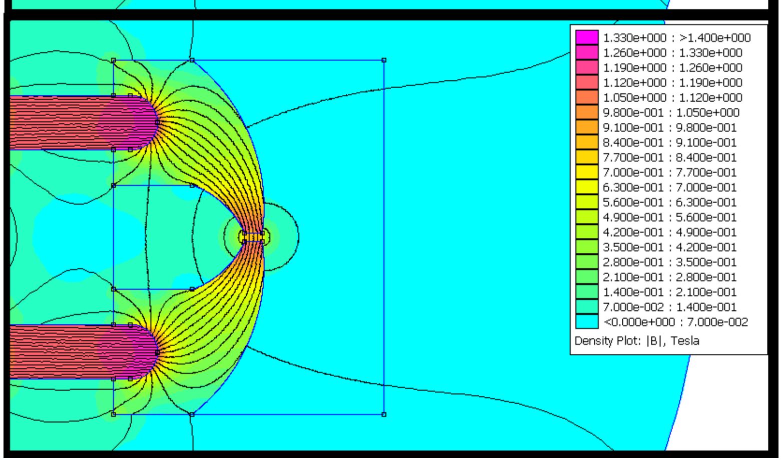
1.330e+000 : >1.400e+000
1.260e+000 : 1.330e+000
1.190e+000 : 1.260e+000
1.120e+000 : 1.190e+000
1.050e+000 : 1.120e+000
9.800e-001 : 1.050e+000
9.100e-001 : 9.800e-001
8.400e-001 : 9.100e-001
7.700e-001 : 8.400e-001
7.000e-001 : 7.700e-001
6.300e-001 : 7.000e-001
5.600e-001 : 6.300e-001
4.900e-001 : 5.600e-001
4.200e-001 : 4.900e-001
3.500e-001 : 4.200e-001
2.800e-001 : 3.500e-001
2.100e-001 : 2.800e-001
1.400e-001 : 2.100e-001
7.000e-002 : 1.400e-001
<0.000e+000 : 7.000e-002
Density Plot: |B|, Tesla

Dependence of $\nabla_x|\vec{B}|$ on parameter o: Outside yoke length

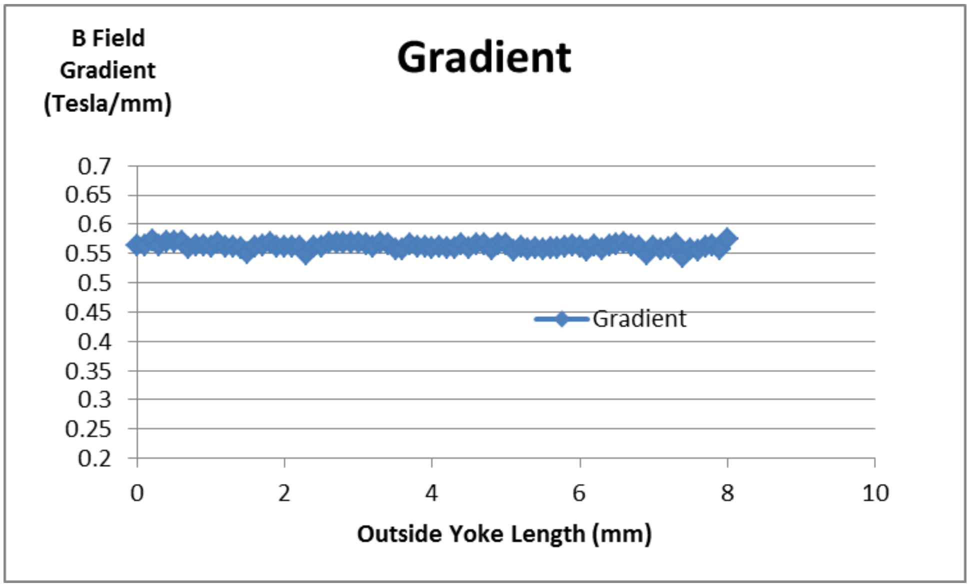

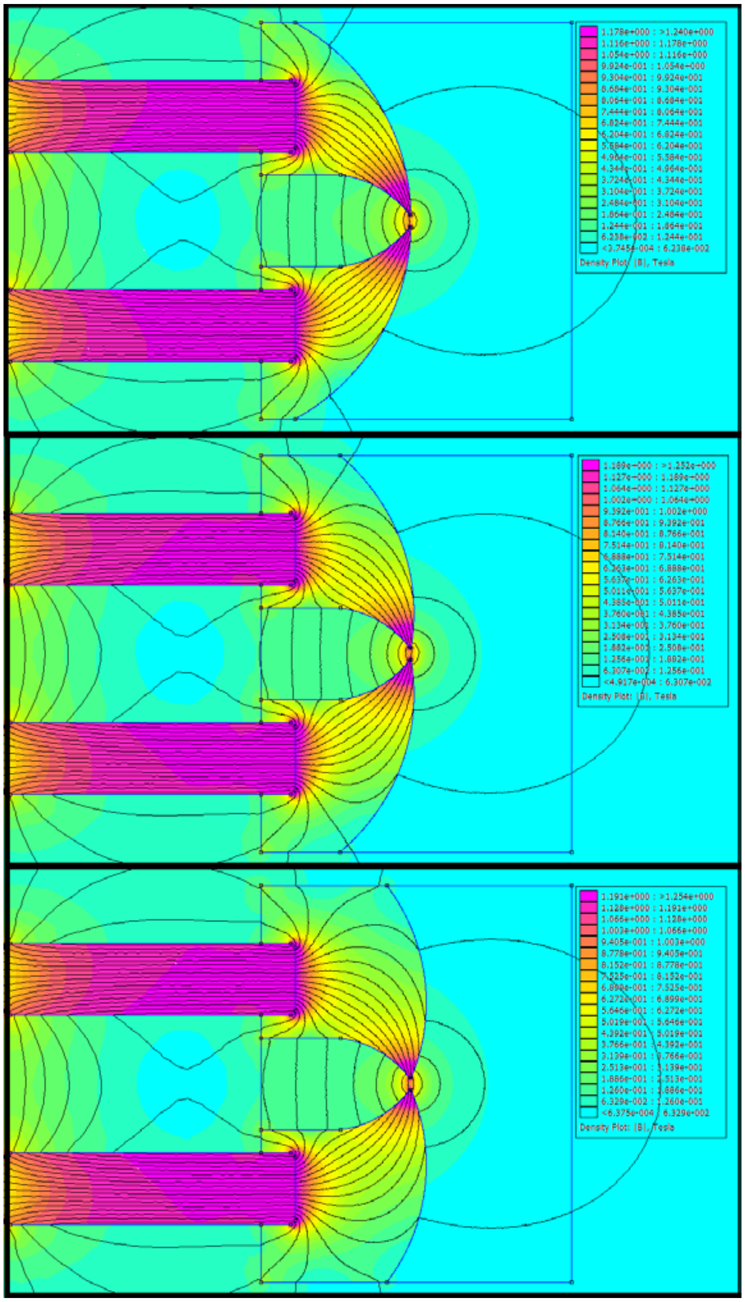
1.178e+000 : >1.240e+000
1.116e+000 : 1.178e+000
1.054e+000 : 1.116e+000
9.924e-001 : 1.054e+000
9.304e-001 : 9.924e-001
8.684e-001 : 9.304e-001
8.064e-001 : 8.684e-001
7.444e-001 : 8.064e-001
6.824e-001 : 7.444e-001
6.204e-001 : 6.824e-001
5.584e-001 : 6.204e-001
4.964e-001 : 5.584e-001
4.344e-001 : 4.964e-001
3.724e-001 : 4.344e-001
3.104e-001 : 3.724e-001
2.484e-001 : 3.104e-001
1.864e-001 : 2.484e-001
1.244e-001 : 1.864e-001
6.238e-002 : 1.244e-001
<3.745e-004 : 6.238e-002
Density Plot: |B|, Tesla
1.189e+000 : >1.252e+000
1.127e+000 : 1.189e+000
1.064e+000 : 1.127e+000
1.002e+000 : 1.064e+000
9.392e-001 : 1.002e+000
8.766e-001 : 9.392e-001
8.140e-001 : 8.766e-001
7.514e-001 : 8.140e-001
6.888e-001 : 7.514e-001
6.263e-001 : 6.888e-001
5.637e-001 : 6.263e-001
5.011e-001 : 5.637e-001
4.385e-001 : 5.011e-001
3.760e-001 : 4.385e-001
3.134e-001 : 3.760e-001
2.508e-001 : 3.134e-001
1.882e-001 : 2.508e-001
1.256e-001 : 1.882e-001
6.307e-002 : 1.256e-001
<4.917e-004 : 6.307e-002
Density Plot: |B|, Tesla
1.191e+000 : >1.254e+000
1.128e+000 : 1.191e+000
1.066e+000 : 1.128e+000
1.003e+000 : 1.066e+000
9.405e-001 : 1.003e+000
8.778e-001 : 9.405e-001
8.152e-001 : 8.778e-001
7.525e-001 : 8.152e-001
6.899e-001 : 7.525e-001
6.272e-001 : 6.899e-001
5.646e-001 : 6.272e-001
5.019e-001 : 5.646e-001
4.392e-001 : 5.019e-001
3.766e-001 : 4.392e-001
3.139e-001 : 3.766e-001
2.513e-001 : 3.139e-001
1.886e-001 : 2.513e-001
1.260e-001 : 1.886e-001
6.329e-002 : 1.260e-001
<6.375e-004 : 6.329e-002
Density Plot: |B|, Tesla

Appendix C: Parts list

Name	Qty	Part #	Company	Price
Mounting Assembly				
6 volt Carbon Zinc battery	1	7690K22	McMaster	$ 5.20
Micrometer Stage	1	M-460P-XYZ-05	Newport	$ 849.99
Actuator	1	L12-I	Firgelli	$ 90.00
Telescopic Slide	1	8379K1	McMaster	$ 89.19
T slot	2 feet	47065T107	McMaster	$ 12.85
Drop-in Fastener with Spring-Loaded Ball	6	47065T226	McMaster	$ 6.72
N50 Neodymium Magnets 3/8 inch Cube	6 x	NB010-N50	http://www.magnet4less.com/	$ 6.84
Controller and interface accessories				
Maple Microcontroller	1	DEV-10664	Sparkfun	$ 44.95
Voltage regulator 5V	2	COM-00107	Sparkfun	$ 2.50
Logic Level Converter	3	BOB-08745	Sparkfun	$ 5.85
Voltage regulator 3.3V	2	COM-00526	Sparkfun	$ 3.90
Breadboard translucent	2	PRT-09567	Sparkfun	$ 11.90
Break Away headers	2	PRT-00116	Sparkfun	$ 3.00
			Total	1982.88

Appendix D: Data sheet for Firgelli linear actuator

Miniature Linear Motion Series · L12

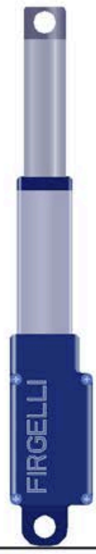

Firgelli Technologies' unique line of Miniature Linear Actuators enables a new generation of motion-enabled product designs, with capabilities that have never before been combined in a device of this size. These small linear actuators are a superior alternative to designing with awkward gears, motors, servos and linkages.

Firgelli's L series of micro linear actuators combine the best features of our existing micro actuator families into a highly flexible, configurable and compact platform with an optional sophisticated on-board microcontroller. The first member of the L series, the L12, is an axial design with a powerful drivetrain and a rectangular cross section for increased rigidity. But by far the most attractive feature of this actuator is the broad spectrum of available configurations.

Benefits

- Compact miniature size
- Simple control using industry standard interfaces
- Low voltage
- Equal push / pull force
- Easy mounting

Applications

- Robotics
- Consumer appliances
- Toys
- Automotive
- Industrial automation

L12 Specifications

Gearing Option	50	100		210
Peak Power Point [1]	12 N @ 11 mm/s	23 N @ 6 mm/s		45 N @ 2.5 mm/s
Peak Efficiency Point	6 N @ 16 mm/s	12 N @ 8 mm/s		18 N @ 4 mm/s
Max Speed (no load)	23 mm/s	12 mm/s		5 mm/s
Backdrive Force [2]	43 N	80 N		150 N
Stroke Option	**10 mm**	**30 mm**	**50 mm**	**100 mm**
Weight	28 g	34 g	40 g	56 g
Positional Accuracy	0.1 mm	0.2 mm	0.2 mm	0.3 mm
Max Side Force (fully extended)	50 N	40 N	30 N	15 N
Mechanical Backlash	0.1 mm			
Feedback Potentiometer	2.75 kΩ/mm ± 30%, 1% linearity			
Duty Cycle	20 %			
Lifetime	1000 hours at rated duty cycle			
Operating Temperature	–10°C to +50°C			
Storage Temperature	–30°C to +70°C			
Ingress Protection Rating	IP-54			
Audible Noise	55 dB at 45 cm			
Stall Current	450 mA at 5 V & 6 V, 200 mA at 12 V			

[1] 1 N (Newton) = 0.225 lb, (pound-force)
[2] a powered-off actuator will statically hold a force up to the Backdrive Force

Dimensions (mm)

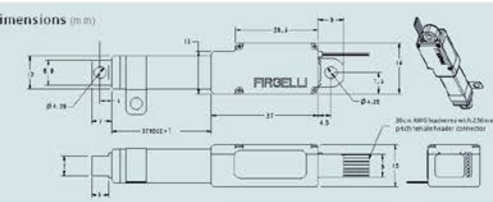

Firgelli Technologies Inc.
4585 Seawood Tce.
Victoria, BC V8N 3W1
Canada

1 (206) 347-9684 *phone*
1 (888) 225-9198 *toll-free*
1 (206) 347-9684 *fax*

sales@firgelli.com
www.firgelli.com

L12 Specifications

Load Curves

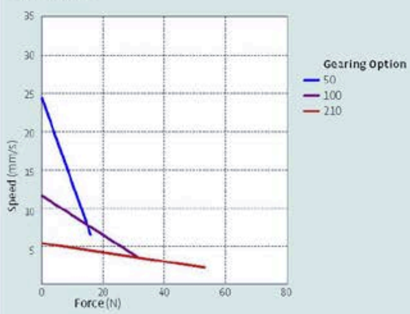

Current Curves

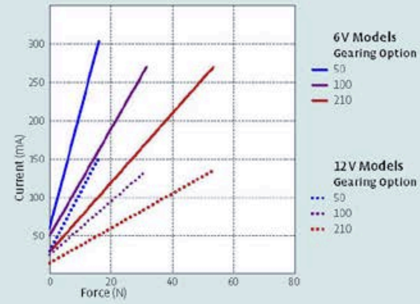

Model Selection

The L12 has five configurable features. L12 configurations are identified according to the following scheme:

L12-SS-GG-VV-C-L

feature	*options*
SS: Stroke Length (in mm)	**10, 30, 50, 100** Any stroke length between 10 and 100mm is available on custom orders, in 2mm increments.
GG: Gear reduction ratio (refer to force/speed plots)	**50, 100, 210** Other gearing options may be possible on custom orders.
VV: Voltage	**06** 6V (5V power for Controller options B and P) **12** 12V
C: Controller	**B** Basic 2-wire open-loop interface, no position feedback, control, or limit switching. Positive voltage extends, negative retracts. **S** 2-wire open-loop interface (like B option) with limit switching at stroke endpoints. **P** Simple analog position feedback signal, no on-board controller. **I** Integrated controller with Industrial and RC servo interfaces (see L12 Controller Options section). Not available with 10mm stroke length configurations. **R** RC Linear Servo. Not available with 10mm stroke or 12 volts.
L: Mechanical or electrical interface customizations	Custom option codes will be issued by Firgelli for custom builds when applicable.

Basis of Operation

The L12 actuator is designed to move push or pull loads along its full stroke length. The speed of travel is determined by the gearing of the actuator and the load or force the actuator is working against at a given point in time (see Load Curves chart on this datasheet). When power is removed, the actuator stops moving and holds its position, unless the applied load exceeds the backdrive force, in which case the actuator will backdrive. Stalling the actuator under power for short periods of time (several seconds) will not damage the actuator. Do not reverse the supply voltage polarity to actuators containing an integrated controller (I controller option).

Each L12 actuator ships with two mounting clamps, two mounting brackets and two rod end options: a clevis end and a threaded end with nut (see drawing on page 4). When changing rod ends, extend the actuator completely and hold the round shaft while unscrewing the rod end. Standard lead wires are 28 AWG, 30 cm long with 2.56 mm (0.1") pitch female header connector (HiTec™ and Futaba™ compatible). Actuators are a sealed unit (IP-54 rating, resistant to dust and water ingress but not fully waterproof).

Ordering information

Sample quantities may be ordered with a credit card directly from www.firgelli.com.

Please contact Firgelli at sales@firgelli.com for volume pricing or custom configurations.

Note that not all configuration combinations are stocked as standard products. Please refer to www.firgelli.com/orders for current inventory.

L12 Controller options

Option B—Basic 2-wire interface

WIRING:

1 (red)	**Motor V+** (5V or 12V)
2 (black)	**Motor ground**

The –B actuators offer no control or feedback mechanisms. While voltage is applied to the motor V+ and ground leads, the actuator extends. If the polarity of this voltage is reversed, the actuator retracts. The 5V actuator is rated for 5V but can operate at 6V.

Option S—Basic 2-wire interface

WIRING:

1 (red)	**Motor V+** (5V or 12V)
2 (black)	**Motor ground**

When the actuator moves to a position within 0.5mm of its fully-retracted or fully-extended stroke endpoint, a limit switch will stop power to the motor. When this occurs, the actuator can only be reversed away from the stroke endpoint. Once the actuator is positioned away from it's stroke endpoint, normal operation resumes. For custom orders, limit switch trigger positions can be modified at the time of manufacture, in 0.5mm increments.

Option P—Position feedback signal

WIRING:

1 (orange)	**Feedback potentiometer negative reference rail**
2 (purple)	**Feedback potentiometer wiper** (position signal)
3 (red)	**Motor V+** (5V or 12V)
4 (black)	**Motor ground**
5 (yellow)	**Feedback potentiometer positive reference rail**

The –P actuators offer no built-in controller, but do provide an analog position feedback signal that can be input to an external controller. While voltage is applied to the motor V+ and ground leads, the actuator extends. If the polarity of this voltage is reversed, the actuator retracts. Actuator stroke position may be monitored by providing any stable low and high reference voltages on leads 1 and 5, and then reading the position signal on lead 2. The voltage on lead 2 will vary linearly between the two reference voltages in proportion to the position of the actuator stroke.

Option I—Integrated controller with industrial and RC servo interfaces

WIRING:

1 (green)	**Current input signal** (used for 4–20 mA interface mode)
2 (blue)	**Voltage input signal** (used for the 0–5V interface mode and PWM interface modes)
3 (purple)	**Position Feedback signal** (0–3.3 V, linearly proportional to actuator position)
4 (white)	**RC input signal** (used for RC-servo compatible interface mode)
5 (red)	**Motor V+** (+6 Vdc for 6 V models, +12 Vdc for 12 V models)
6 (black)	**Ground**

The –I actuator models feature an on-board software-based digital microcontroller. The microcontroller is not user-programmable.

The six lead wires are split into two connectors. Leads 4, 5 and 6 terminate at a universal RC servo three-pin connector (Hi-Tec™ and Futaba™ compatible). Leads 1, 2 and 3 terminate at a separate, similarly sized connector.

When the actuator is powered up, it will repeatedly scan leads 1, 2, 4 for an input signal that is valid under any of the four supported interface modes. When a valid signal is detected, the actuator will self-configure to the corresponding interface mode, and all other interface modes and input leads are disabled until the actuator is next powered on.

0–5 V Interface Mode: This mode allows the actuator to be controlled with just a battery, and a potentiometer to signal the desired position to the actuator – a simple interface for prototypes or home automation projects. The desired actuator position (setpoint) is input to the actuator on lead 2 as a voltage between ground and 5V. The setpoint voltage must be held on lead 2 until the desired actuator stroke position is reached. Lead 2 is a high impedance input.

4–20 mA Interface Mode: This mode is compatible with PLC devices typically used in industrial control applications. The desired actuator position (setpoint) is input to the actuator on lead 1 as a current between 4 mA and 20 mA. The setpoint current must be held on lead 1 until the desired actuator stroke position is reached.

RC Servo Interface Mode: This is a standard hobby-type remote-control digital servo interface (CMOS logic), compatible with servos and receivers from manufacturers like Futaba™ and Hi-Tec™. The desired actuator position is input to the actuator on lead 4 as a positive 5 Volt pulse width signal. A 1.0 ms pulse commands the controller to fully retract the actuator, and a 2.0 ms pulse signals full extension. If the motion of the actuator, or of other servos in your system, seems erratic, place a 1–4Ω resistor in series with the actuator's red V+ leadwire.

PWM Mode: This mode allows control of the actuator using a single digital output pin from an external microcontroller. The desired actuator position is encoded as the duty cycle of a 5 Volt 1 kHz square wave on actuator lead 2, where the % duty cycle sets the actuator position to the same % of full stroke extension. The waveform must be 0V to +5V in order to access the full stroke range of the actuator.

Option R—RC Linear Servo

WIRING:

1 (white)	**RC input signal**
2 (red)	**Motor V+** (6VOC)
3 (black)	**Ground**

The –R actuators or 'linear servos' are a direct replacement for regular radio controlled hobby servos. Operation is as above in RC servo interface mode (option I). The –R actuators are available in 6 volt and 30, 50 and 100 mm strokes only.

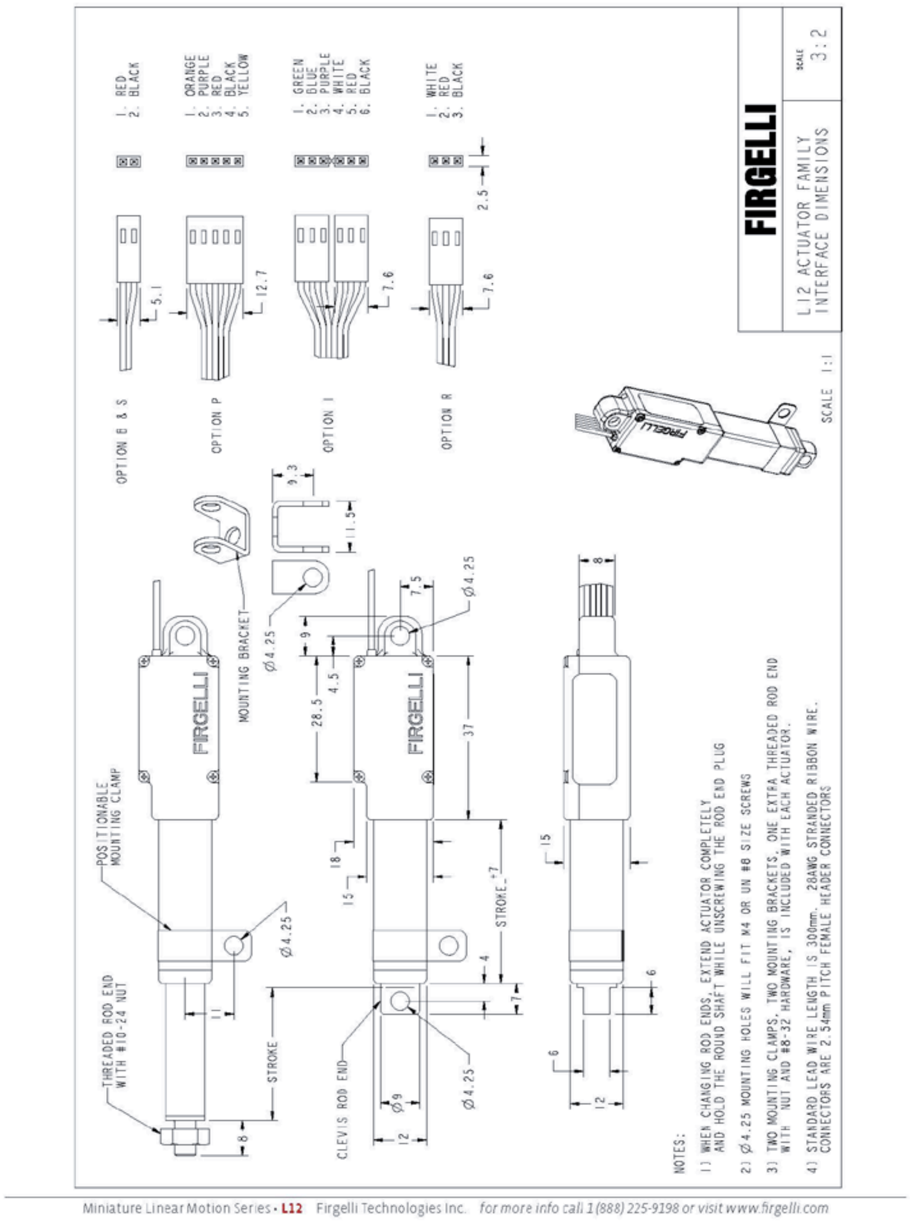
FIRGELLI
L12 ACTUATOR FAMILY
INTERFACE DIMENSIONS
SCALE 3:2
OPTION B & S
1. RED
2. BLACK
OPTION P
1. ORANGE
2. PURPLE
3. RED
4. BLACK
5. YELLOW
OPTION I
1. GREEN
2. BLUE
3. PURPLE
4. WHITE
5. RED
6. BLACK
OPTION R
1. WHITE
2. RED
3. BLACK
MOUNTING BRACKET
POSITIONABLE MOUNTING CLAMP
THREADED ROD END WITH #10-24 NUT
CLEVIS ROD END
STROKE
SCALE 1:1
NOTES:
1) WHEN CHANGING ROD ENDS, EXTEND ACTUATOR COMPLETELY AND HOLD THE ROUND SHAFT WHILE UNSCREWING THE ROD END PLUG
2) Ø4.25 MOUNTING HOLES WILL FIT M4 OR UN #8 SIZE SCREWS
3) TWO MOUNTING CLAMPS, TWO MOUNTING BRACKETS, ONE EXTRA THREADED ROD END WITH NUT AND #8-32 HARDWARE, IS INCLUDED WITH EACH ACTUATOR.
4) STANDARD LEAD WIRE LENGTH IS 300mm. 28AWG STRANDED RIBBON WIRE. CONNECTORS ARE 2.54mm PITCH FEMALE HEADER CONNECTORS
Miniature Linear Motion Series • L12 Firgelli Technologies Inc. for more info call 1 (888) 225-9198 or visit www.firgelli.com

Appendix E: Magnetic Circuit Model

When designing a magnet and yoke array, a simple mathematical model can be used to gain a first order approximation of the system's magnetic properties and behaviors. This can be accomplished using magnetic circuit modeling. By developing a mathematical model of this kind, major changes in materials and geometry can be assessed quickly and easily, providing insights into best practises when designing a magnetic tweezers device.

A magnetic circuit model can easily provide an estimate of the magnetic flux (B field) in the air gap between the yoke tips of the magnetic tweezers device.

Before developing a circuit model, it is helpful to review and define some terms that will be employed in the modeling of this system.

Φ is the total magnetic flux passing through a surface. It is defined as the surface integral of the magnetic flux density B and the area of the surface through which B is passing.

$$\varphi = \int B \cdot dA$$

B in this case is the magnetic flux density and A is the surface area through which B passes. If Φ is assumed to be uniform everywhere on the surface A, then the expression for Φ becomes

$$\varphi = B \cdot dA$$

In solving magnetic circuit models it is useful to use the Magnetomotive Force (MMF) represented by the symbol F. The MMF is analogous to the electromotive force in electrical circuits and can be viewed as the source of magnetic fields. The MMF is a potential and must be defined be defined between two points. The MMF is related to the magnetic field H through the path integral between a start and an end point.

$$F = \int H \cdot dl$$

If a uniform H field is assumed, the integral sign can be dropped and the expression for F becomes

$$F = H \cdot l$$

Where l is the length of the path integral.

F can also be related to the total magnetic flux by a quantity known as magnetic reluctance, R.

$$F = \varphi \cdot R$$

The reluctance is analogous to resistance in electrical circuits. However, instead of a measure of electrical energy dissipation, the reluctance is a measure of a circuit, or circuit element's ability to store magnetic energy. The reluctance of a circuit element can be expressed in terms of the cross sectional area of the element, the length of the element and the permeability of the element.

$$R = \frac{L}{\mu \cdot A}$$

Sometimes in magnetic circuit analysis, it is more useful to use the inverse of reluctance, which is called magnetic permanence P.

$$P = \frac{1}{R} = \frac{\mu \cdot A}{L}$$

Finally we remember that the magnetic field H is related to the magnetic flux density B through the following

$$H = \frac{B}{\mu}$$

Where μ is the permeability.

We can now proceed with a simplified circuit model of our magnetic tweezers device in which we will derive an estimate for the B field between the yoke tips. We will make a few simplifying assumptions to make the analysis easier. The first assumption is that the magnetic losses due to the circuit elements are negligible. This assumption means that the flux calculated will be a maximum flux which the real system will certainly fall short of. A second assumption is that the average path of the magnetic flux is along the centerline of each element composing the magnet-yoke array. A third assumption is that the horn shaped yokes are simple and uniformly shaped so that the magnetic flux inside the yokes trace out a 45 degrees of a turn. A final assumption is that each element in the system is below its magnetic saturation. This is important to maintain the linearity of the model. Each of these assumptions will lead to error in the prediction of the model, however, the model can used to study global changes in the magnet and yoke geometry and composition. Additionally, each of these assumptions is addressed by the application of numerical methods to solve for the magnetic circuit without simplifying assumptions.

One useful application of this magnetic circuit model is to examine the large changes to the array composition, for example, the effects of changing the material which is placed on the opposite side of the horned yokes. Let us take the cases shown in Appendix E Figure 18 A and B. Panel A shows a magnetic tweezers design which uses a steel backing while panel B shows a design which uses an additional magnet at the back of the device in order to increase the magnetic flux at the tips (in the air gap).

Using just steel and permanent magnets, the line integral

$$F = \int H \cdot dl$$

Around a closed loop in the magnetic circuit must be zero.

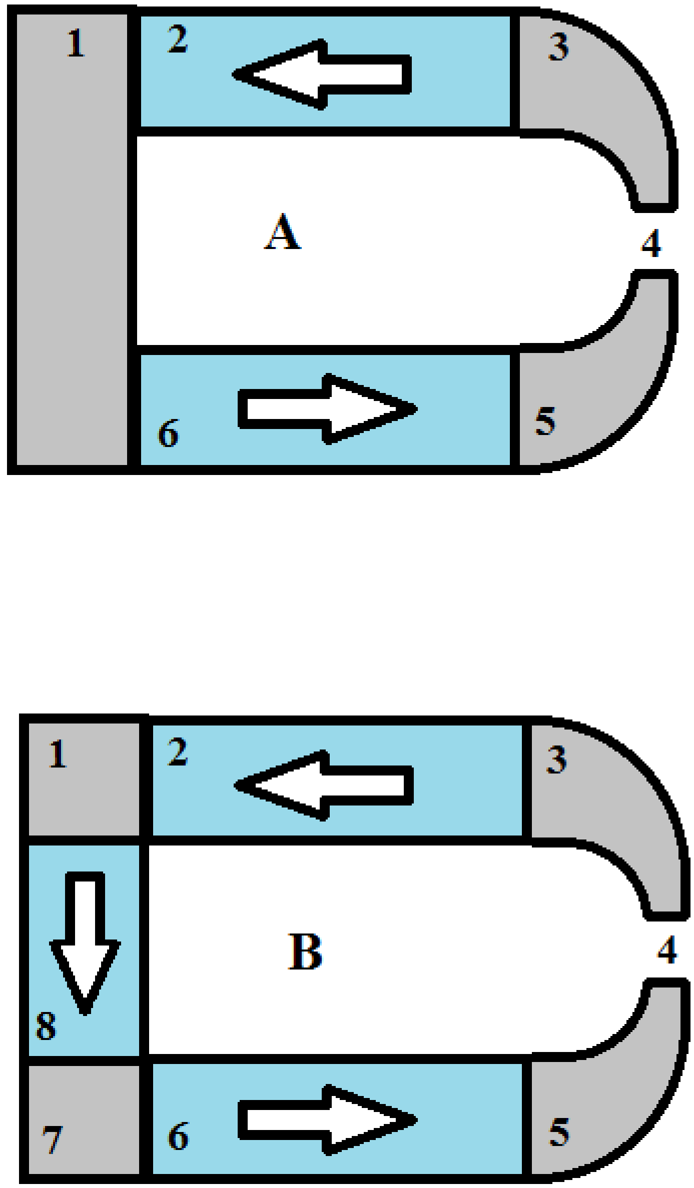

Appendix E Figure 18: Case A and B for examination using magnetic circuit modeling. The blue elements are permanent magnets with arrows facing the north pole of the magnet. The gray elements are made of steel. Configuration A has a piece of steel as a backing while configuration B has two pieces of steel to help steer the magnetic fields and a third magnet in

order to add to the magnetomotive force in the circuit. Circuit elements are numbered in each panel to facilitate calculation of flux through each element individually.

This means that the following must be true This means that the following must be true

$$H_1L_1 + H_2L_2 + H_3L_3 + H_4L_4 + H_5L_5 + H_6L_6 = 0$$

Of course we remember that the direction of the H field in a permanent magnet is opposite that which it induces in other materials, thus magnetic H_2 and H_6 are negative quantities. A magnetic circuit diagram can be created for this simple case and is shown in

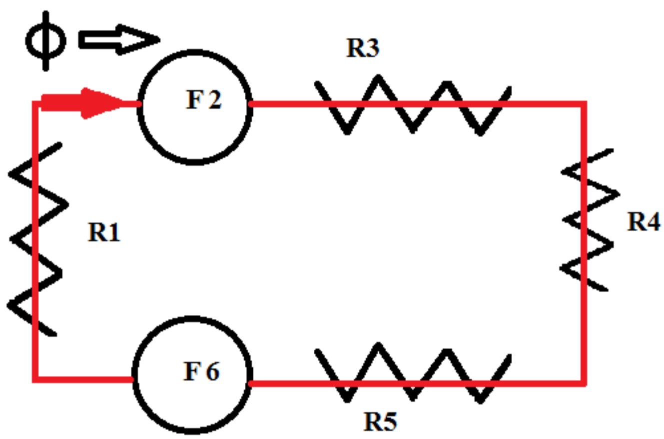

Appendix E Figure 19: A magnetic circuit model of the magnetic tweezers design shown in Appendix E Figure 18 panel A.

From the relations given above we can derive the H values in terms of total flux and the properties of each circuit element.

$$H_1 = \frac{B_1}{\mu_1} = \frac{\varphi_1}{\mu_1 \cdot A_1}$$

A similar relation can be written for each circuit element. The total flux through the magnetic circuit remains constant though $\varphi_1 = \varphi_2 = \varphi_3 = \cdots = \varphi_{total}$

Since $\varphi_1 = B_1 \cdot A_1$ ... it stands to reason that $B_1 \cdot A_1 = B_2 \cdot A_2 = B_3 \cdot A_3 = \cdots$

Here of course the cross sectional area of the horned yokes is not constant. If we neglect leakage flux, then the B field in the yokes should increase as A decreases, and the product of the two should remain constant. For simplicity, the value of B and A in the horned yokes can just be assigned the average value of those quantities in the yoke.

By combining the above equations, and with a little manipulation, we can derive an equation for the value of B in panel A, in the gap between the yoke tips (region 4), assuming the magnets are identical in strength and length.

$$B_4^A = \frac{2 \cdot H_2 L_2}{A_4 \left[\frac{L_1}{\mu_1 A_1} + \frac{L_3}{\mu_3 A_3} + \frac{L_4}{\mu_4 A_4} + \frac{L_5}{\mu_5 A_5}\right]}$$

As we can see from the above equation, in order to maximize B_4^A we would like to minimize A_4 , L_1, L_2, L_4 and L_5. Neglecting losses and saturation, we would also like to maximize the areas of circuit elements 1, 3, and 5. 4

We can now perform a similar analysis on panel B, the case where there is a magnet on the back of the magnetic tweezers device. In this case * will denote the lengths of elements 1, 7 and 8 as a reminder that they sum to the original L_1.

$$B_4^B = \frac{(2 \cdot H_2 L_2) + H_8 L_8^*}{A_4 \left[\frac{L_1^*}{\mu_1 A_1} + \frac{L_3}{\mu_3 A_3} + \frac{L_4}{\mu_4 A_4} + \frac{L_5}{\mu_5 A_5} + \frac{L_7^*}{\mu_7 A_7}\right]}$$

If we let all the circuit elements other than those in regions 1, 7 and 8 remain constant, and replace L_1 for $(L_1^* + L_7^* + L_8^*)$ we can simplify the expressions for B_4^A and B_4^B.

$$B_4^A = \frac{C1}{[L_1^* + L_7^* + L_8^* + C2]}$$

And

$$B_4^B = \frac{C1 + H_8 L_8^*}{[L_1^* + L_7^* + C2]}$$

The inevitable conclusion is that the magnet at the back is of great benefit to producing a high B field near the yoke tips. Of course there were simplifications made with this model, but the details can be solved for numerically.